ISSN 1054-660X, Laser Physics, 2006, Vol. 16, No. 10, pp. 1451–1477.

Classical and Quantum Aspects of Multimode Parametric Interactions

A. Allevi[a, *], M. Bondani[b], A. Ferraro[c, d], and M. G. A. Paris[c]

[a] *Dipartimento di Fisica e Matematica, Università degli Studi dell'Insubria and Consiglio Nazionale delle Ricerche, Istituto Nazionale per la Fisica della Materia, Como, I-22100 Italy*

[b] *National Laboratory for Ultrafast and Ultraintense Optical Science, Consiglio Nazionale delle Ricerche, Istituto Nazionale per la Fisica della Materia, Como, I-22100 Italy*

[c] *Dipartimento di Fisica dell'Università di Milano, Milano, I-20133 Italy*

[d] *ICFO—Institut de Ciències Fotòniques, E-08860 Castelldefels, Barcelona, Spain*

*e-mail: alessia.allevi@uninsubria.it

Received May 6, 2006

Abstract—Parametric interactions in nonlinear crystals represent a powerful tool in the optical manipulation of information, both in the classical and the quantum regime. Here, we analyze in detail classical and quantum aspects of three- and five-mode parametric interactions in $\chi^{(2)}$ nonlinear crystals. The equations of motion are explicitly derived and then solved within the parametric approximation. We describe several applications, including holography, all-optical gates, generation of entanglement, and telecloning. Experimental results on the photon distributions and correlations of the generated beams are also reported and discussed.

PACS numbers: 42.65.Yj, 03.67.Mn, 42.65.Lm, 42.40.-i, 42.50.Nn, 42.50.Dv

DOI: 10.1134/S1054660X06100082

1. INTRODUCTION

The parametric nonlinear interaction between light waves [1, 2], as, for example, the creation of the second harmonic [3], has been studied since the discovery of the laser. In particular, the interactions of different radiation modes in nonlinear $\chi^{(2)}$ crystals give rise to several interesting effects, such as multiwave mixing, up- and downconversion, self-phase modulation, cross-phase modulation, and frequency doubling. At the output of a nonlinear crystal, one may find many different states of light, which themselves exhibit a rich variety of phenomena [4–18] both in the classical and in the quantum domain. As a matter of fact, nonlinear effects in $\chi^{(2)}$ crystals represent one of the most efficient systems to manipulate optical beams, both in the temporal and in the spatial domain. Indeed, even if $\chi^{(2)}$ nonlinearity is weak compared to a quasiresonant interaction with atoms, the excess noise in the process is very low. The parametric amplification, compared to the laser mechanism, is broadband and, in the case of pulsed pumping, may achieve high gain per unit length. Moreover, the gain bandwidth is determined by the dispersive properties and by the length of the crystal rather than by details of a laser transition and does not involve energy storage.

As mentioned above, nonlinearities of $\chi^{(2)}$ crystals are generally small, and, thus, the above effects become relevant only when high-power beams impinge onto the crystal. As a consequence, in nonlinear interactions of this kind, one or more of the involved modes should provide the energy needed to enhance the nonlinear effects. Those modes, globally referred to as pumps, are excited in high-amplitude coherent states by some suitable laser source. The pump modes are only slightly affected by the interactions, and, as a result, the parametric approximation is widely used to compute the dynamical evolution [19]. In the parametric approximation, which is accurately verified in many regimes, one assumes that the pump modes remain undepleted and/or Poissonian during the evolution [20]. This assumption allows one to ignore the pumps' evolution in the classical equations or, in the quantum regime, to classically treat them as a c number, thus neglecting their quantum fluctuations. As a result, one or more classical equations may be ignored, whereas, in the quantum regime, trilinear Hamiltonians are reduced to quadratic forms in the field operators, and, hence, some useful mathematical tools, typically decomposition formulas for Lie algebras, can be exploited for calculations [6, 21–24].

Classical analysis of nonlinear interactions often provides a good description of experimental results, while it fails when spontaneous processes become relevant, as, for example, during the process of downconversion, which leads to generation of entangled beams of light. In addition, although the classical approach cannot account for the genuine quantum properties of the output beams, it is worthwhile to perform a classical analysis of the system with the aim of obtaining a reliable identification between classical and quantum parameters, which serves as a guide in order to design a proper experimental implementation.

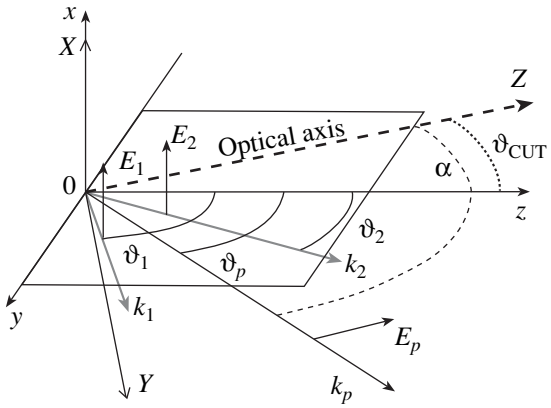

Fig. 1. Noncollinear three-wave interaction in a type-I uniaxial crystal (X, Y, Z): crystal reference frame with Z parallel to the optical axis; (x, y, z), laboratory reference frame with the (x, y) plane coinciding with the crystal entrance face; α, tuning angle; ϑ_{CUT}, cut angle. The plane (y, z) is the principal plane for all the interacting waves.

In this paper, we analyze in detail classical three- and five-mode parametric interactions in $\chi^{(2)}$ crystals, as well as the corresponding bilinear two- and three-mode quantum models. Section 2 is devoted to three-mode interactions. The classical evolution equations are explicitly derived and then solved within the parametric approximation, taking into account phase mismatching either in modulus or in direction. The quantum description of the interaction is given in Section 2.2, where the generation of entanglement is also analyzed. In Sections 2.3 and 2.4, we discuss the generation of a twin beam, with focus on the statistical distributions and photon correlations, and report experimental results obtained with BBO crystals. Section 3 analyzes five-mode interactions, both in the classical and in the quantum regimes. Applications of five-mode interactions to holography, logic gates, generation of three-mode entanglement, and telecloning are described with some details in Sections 3.2, 3.3, 3.4, and 3.5, respectively. Experimental results concerning statistical distributions and photon correlations of the generated beams are reported and discussed in Sections 3.6 and 3.7. Finally, Section 4 closes the paper with some concluding remarks.

2. THREE-MODE PARAMETRIC PROCESSES

In this section, we address the interaction among three modes of the radiation field. First, we analyze in detail the classical evolution, giving attention to phase-mismatching effects. Then we describe, within the parametric approximation, the resulting two-mode quantum evolution, which leads to the generation of the so-called entangled twin beam (TWB) state of radiation. Experimental results concerning TWB generation and measurements of correlation are reported in the last two subsections.

2.1. Classical Evolution

A nonlinear optical process may be viewed as being realized in two steps: first, the intense light emitted by a laser source induces a nonlinear response [26]. Then, the medium, in reacting to the external field, modifies the optical field in a nonlinear way. The relation between the dielectric polarization $\mathbf{P}$ and the optical electric field $\mathbf{E}$ can thus be written as

$$\begin{aligned}\mathbf{P} &= \epsilon_0\chi\mathbf{E} + 2d\mathbf{EE} + 4\chi^{(3)}\mathbf{EEE} + \ldots \\ &= \epsilon_0\chi\mathbf{E} + \mathbf{P}_{NL},\end{aligned} \tag{1}$$

in which ϵ_0 is the vacuum dielectric constant and d and $\chi^{(3)}$ are coefficients that describe the second- and third-order nonlinear effects, respectively [27]. In the following we will only consider the second-order nonlinearity.

The propagation of light in an arbitrary homogeneous dielectric medium reads as follows:

$$\nabla^2\mathbf{E} - \frac{1}{c^2}\frac{\partial^2\mathbf{E}}{\partial t^2} = -\mathbf{S}, \tag{2}$$

in which

$$\mathbf{S} = -\mu_0\frac{\partial^2\mathbf{P}_{NL}}{\partial t^2} \tag{3}$$

plays the role of a source radiating in a linear medium of refractive index n, $c = c_0/n$ is the speed of light in the medium with c_0 and μ_0 the light velocity and the magnetic permeability of free space, respectively.

Suppose that the medium is a β-BaB_2O_4 crystal (BBO), that is, a birefringent uniaxial negative crystal, and that $\mathbf{E}$ is a superposition of three plane waves $\mathbf{E}_1$, $\mathbf{E}_2$, and $\mathbf{E}_p$ of angular frequencies ω_1, ω_2, and ω_p. In Fig. 1, the fields $\mathbf{E}_1$ and $\mathbf{E}_2$ are directed along the x axis (ordinarily polarized), while the field $\mathbf{E}_p$ lies in the (y, z) plane (extraordinarily polarized) [28]. Let us assume that the three wave vectors $\mathbf{k}_j$ propagate at different angles ϑ_j to direction z, in the (y, z) plane of the crystal, also containing the optical axis. We can thus write the fields interacting at position $\mathbf{r} = (x, y, z)$ in any plane at fixed x, say, $x = 0$, as follows:

$$\begin{aligned}\mathbf{E}_1(\mathbf{r}, t) &= \frac{\hat{\mathbf{x}}}{2}\{A_1 a_1(\mathbf{r})e^{-i\phi_1} + \text{c.c.}\}, \\ \mathbf{E}_2(\mathbf{r}, t) &= \frac{\hat{\mathbf{x}}}{2}\{A_2 a_2(\mathbf{r})e^{-i\phi_2} + \text{c.c.}\}, \\ \mathbf{E}_3(\mathbf{r}, t) &= \frac{1}{2}\{A_3[\hat{\mathbf{y}}a_{py}(\mathbf{r}) + \hat{\mathbf{z}}a_{pz}(\mathbf{r})]e^{-i\phi_p} + \text{c.c.}\},\end{aligned} \tag{4}$$

where $A_j = (2\eta_0\hbar\omega_j/n_j)(1/2)$, $\phi_j = k_j z\cos\vartheta_j + k_j y\sin\vartheta_j - \omega_j t$, $j = 1, 2, p$, and $\hat{\mathbf{x}}$, $\hat{\mathbf{y}}$, $\hat{\mathbf{z}}$ denote the directions of the

axes. The total field inside the crystal is given by

$$\begin{aligned}\mathbf{E} &= \mathbf{E}_1 + \mathbf{E}_2 + \mathbf{E}_p \\ &= (E_1 + E_2)\hat{\mathbf{x}} + E_{py}\hat{\mathbf{y}} + E_{pz}\hat{\mathbf{z}} + \text{c.c.}\end{aligned} \tag{5}$$

If we suppose that the angular frequencies are commensurate, for instance, $\omega_1 + \omega_2 = \omega_p$ (frequency-matching condition), then, by considering the components of Eq. (2) in the laboratory frame (x, y, z), we obtain the following system of equations:

$$\nabla^2(E_1 + E_2) - \frac{1}{c^2}\frac{\partial^2(E_1 + E_2)}{\partial t^2} = \mu_0\frac{\partial^2 \mathbf{P}_{NL}\cdot\hat{\mathbf{x}}}{\partial t^2}, \tag{6a}$$

$$\nabla^2 E_{py} - \frac{1}{c^2}\frac{\partial^2 E_{py}}{\partial t^2} = \mu_0\frac{\partial^2 \mathbf{P}_{NL}\cdot\hat{\mathbf{y}}}{\partial t^2}, \tag{6b}$$

$$\nabla^2 E_{pz} - \frac{1}{c^2}\frac{\partial^2 E_{pz}}{\partial t^2} = \mu_0\frac{\partial^2 \mathbf{P}_{NL}\cdot\hat{\mathbf{z}}}{\partial t^2}. \tag{6c}$$

The second members of these equations contain a number of terms at different frequencies, while each term in the first members only depends on one of the frequencies ω_1, ω_2, and ω_p. Thus, by equating the terms at the same frequencies, we get

$$\nabla^2 E_1 - \frac{1}{c^2}\frac{\partial^2 E_1}{\partial t^2} = 4\omega_1^2[d_+E_{py} + d_-E_{pz}]E_2^*, \tag{7a}$$

$$\nabla^2 E_2 - \frac{1}{c^2}\frac{\partial^2 E_2}{\partial t^2} = 4\omega_2^2[d_+E_{py} + d_-E_{pz}]E_1^*, \tag{7b}$$

$$\nabla^2 E_{py} - \frac{1}{c^2}\frac{\partial^2 E_{py}}{\partial t^2} = 4\omega_p^2 d_+E_1E_2, \tag{7c}$$

$$\nabla^2 E_{pz} - \frac{1}{c^2}\frac{\partial^2 E_{pz}}{\partial t^2} = 4\omega_p^2 d_-E_1E_2, \tag{7d}$$

where we have defined

$$d_+ = d_{22}\cos(\alpha - \vartheta_p) + d_{31}\sin(\alpha - \vartheta_p), \tag{8a}$$

$$d_- = d_{22}\sin(\alpha - \vartheta_p) - d_{31}\cos(\alpha - \vartheta_p). \tag{8b}$$

By substituting into Eqs. (7) the expressions for fields E_1, E_2, and E_p given by Eqs. (5) and by assuming that the complex amplitudes $a_q(z)$ are slowly varying with z, we obtain

$$\begin{aligned}&\hat{\mathbf{k}}_1\cdot\nabla a_1(\mathbf{r}) \\ &= i[g_+a_{py}(\mathbf{r}) + g_-a_{pz}(\mathbf{r})]a_2^*(\mathbf{r})e^{-i\Delta\mathbf{k}\cdot\mathbf{r}},\end{aligned} \tag{9a}$$

$$\begin{aligned}&\hat{\mathbf{k}}_2\cdot\nabla a_2(\mathbf{r}) \\ &= i[g_+a_{py}(\mathbf{r}) + g_-a_{pz}(\mathbf{r})]a_1^*(\mathbf{r})e^{-i\Delta\mathbf{k}\cdot\mathbf{r}},\end{aligned} \tag{9b}$$

$$\hat{\mathbf{k}}_p\cdot\nabla a_{py}(\mathbf{r}) = ig_+a_1(\mathbf{r})a_2(\mathbf{r})e^{-i\Delta\mathbf{k}\cdot\mathbf{r}}, \tag{9c}$$

$$\hat{\mathbf{k}}_p\cdot\nabla a_{pz}(\mathbf{r}) = ig_-a_1(\mathbf{r})a_2(\mathbf{r})e^{-i\Delta\mathbf{k}\cdot\mathbf{r}}, \tag{9d}$$

where $\Delta k = \mathbf{k}_p - \mathbf{k}_1 - \mathbf{k}_2$ denotes the phase mismatch, $\nabla = \hat{\mathbf{y}}\partial_y + \hat{\mathbf{z}}\partial_z$ and $g_\pm = d_\pm[(2\hbar\omega_1\omega_2\omega_p\eta_0^3)/(n_1n_2n_p)]^{1/2}$ are real coupling constants. In order to solve system (9), it is necessary to make some assumptions; in particular, we suppose that the field a_p remains undepleted during the interaction, namely, $A_p(\mathbf{r}) = g_+a_{py}(\mathbf{r}) + g_-a_{pz}(\mathbf{r}) = A_p(0)$. Under this hypothesis, system (9) reduces to two equations that can be analytically solved:

$$\begin{aligned}a_1(\mathbf{r}) &= \exp\left(-i\frac{\Delta\mathbf{k}}{2}\cdot\mathbf{r}\right)\left\{a_1(0)\cosh\left(Q\frac{\hat{\Delta\mathbf{k}}}{2}\cdot\mathbf{r}\right)\right. \\ &\left. + \frac{i}{Q}\left[\Delta k a_1(0) + \frac{2A_p(0)}{\hat{\Delta\mathbf{k}}\cdot\hat{\mathbf{k}}_1}a_2^*(0)\right]\sinh\left(Q\frac{\hat{\Delta\mathbf{k}}}{2}\cdot\mathbf{r}\right)\right\},\end{aligned} \tag{10a}$$

$$\begin{aligned}a_2(\mathbf{r}) &= \exp\left(-i\frac{\Delta\mathbf{k}}{2}\cdot\mathbf{r}\right)\left\{a_2(0)\cosh\left(Q\frac{\hat{\Delta\mathbf{k}}}{2}\cdot\mathbf{r}\right)\right. \\ &\left. + \frac{i}{Q}\left[\Delta k a_2(0) + \frac{2A_p(0)}{\hat{\Delta\mathbf{k}}\cdot\hat{\mathbf{k}}_2}a_1^*(0)\right]\sinh\left(Q\frac{\hat{\Delta\mathbf{k}}}{2}\cdot\mathbf{r}\right)\right\},\end{aligned} \tag{10b}$$

in which the parameter Q is defined as

$$Q = \sqrt{\frac{4|A_p(0)|^2}{(\hat{\Delta\mathbf{k}}\cdot\hat{\mathbf{k}}_1)(\hat{\Delta\mathbf{k}}\cdot\hat{\mathbf{k}}_2)} - \Delta k^2}. \tag{11}$$

For historical reasons, a_1 and a_2 are usually called "signal" and "idler." If we inject the crystal with two fields only, that is, the pump field a_p and the seed field $a_1(0)$, the solutions in Eqs. (10a) and (10b) reduce to

$$\begin{aligned}a_1(\mathbf{r}) &= a_1(0)\left\{\cosh\left(Q\frac{\hat{\Delta\mathbf{k}}}{2}\cdot\hat{\mathbf{r}}\right)\right. \\ &\left. + i\frac{\Delta k}{Q}\sinh\left(Q\frac{\hat{\Delta\mathbf{k}}}{2}\cdot\hat{\mathbf{r}}\right)\right\}\exp\left(-i\frac{\hat{\Delta\mathbf{k}}}{2}\cdot\hat{\mathbf{r}}\right),\end{aligned} \tag{12a}$$

$$\begin{aligned}a_2(\mathbf{r}) &= \frac{2iA_p(0)a_1^*(0)}{Q(\hat{\Delta\mathbf{k}}\cdot\hat{\mathbf{k}}_2)} \\ &\times \sinh\left(Q\frac{\hat{\Delta\mathbf{k}}}{2}\cdot\hat{\mathbf{r}}\right)\exp\left(-i\frac{\hat{\Delta\mathbf{k}}}{2}\cdot\hat{\mathbf{r}}\right).\end{aligned} \tag{12b}$$

Equation (12b) shows that the generated field $a_2(\mathbf{r})$ depends on the conjugate of the seed field $a_1(0)$: as we have shown in previous works (see, for example, [28, 29]), this dependence can be interpreted as the result of the holographic nature of three-wave mixing. In fact, if we put an object on the seed field $a_1(0)$ and consider the pump field a_p as the reference field, $a_2(z)$, being propor-

tional to $a_1^*(0)$, reconstructs a real holographic image of the object.

Moreover, from the solution for field $a_1(\mathbf{r})$, we can derive the gain of the nonlinear interaction

$$\Gamma = \frac{|a_1(\mathbf{r})|^2 - |a_1(0)|^2}{|a_1(0)|^2} = \frac{4|A_p(0)|^2}{Q^2(\Delta\hat{\mathbf{k}}\cdot\hat{\mathbf{k}}_1)(\Delta\hat{\mathbf{k}}\cdot\hat{\mathbf{k}}_2)}\sinh^2\left(Q\frac{\Delta\mathbf{k}}{2}\cdot\mathbf{r}\right). \quad (13)$$

Since from an experimental point of view we will observe the amplified field $a_1(\mathbf{r})$, we can choose $\mathbf{r} = L\hat{\mathbf{k}}_1$, where L represents the effective length of the crystal, in which the amplification of the signal occurs.

Note that the conversion efficiency is maximized when the phase-matching condition is satisfied, that is, $\mathbf{k}_p = \mathbf{k}_1 + \mathbf{k}_2$.

2.1.1. Phase mismatching in modulus. As we have seen in the previous subsection, it is possible to generate light even in phase-mismatching conditions. In order to better investigate this point, here we will discuss separately the cases of phase mismatch in modulus and in direction, for small deviations from the phase-matching condition. First, we analyze the case of a noncollinear interaction for small deviations in the modulus of the wave vectors that interact inside the crystal. Let us expand the phase mismatching $\Delta\mathbf{k}$ in a Taylor series up to the second order of the expansion of k_1 about $\bar{\omega}_1$ and of k_2 about $\bar{\omega}_2$, where each $\bar{\omega}_j$ represents the central frequency of the field a_j:

$$\begin{aligned}\Delta\mathbf{k} &= \frac{1}{c_0}(n_p\omega_p\hat{\mathbf{k}}_p - n_1\bar{\omega}_1\hat{\mathbf{k}}_1 - n_2\bar{\omega}_2\hat{\mathbf{k}}_2)\\ &= \frac{1}{c_0}\left\{-\left[\left(\frac{\partial n_1}{\partial\omega}\right)_{\bar{\omega}_1}\bar{\omega}_1 + n_1(\bar{\omega}_1)\right]\hat{\mathbf{k}}_1\right.\\ &\quad \left.+\left[\left(\frac{\partial n_2}{\partial\omega}\right)_{\bar{\omega}_2}\bar{\omega}_2 + n_2(\bar{\omega}_2)\right]\hat{\mathbf{k}}_2\right\}\delta\omega \quad (14)\\ &\quad +\frac{1}{c_0}\left\{-\left[\left(\frac{\partial^2 n_1}{\partial\omega^2}\right)_{\bar{\omega}_1}\bar{\omega}_1 + 2\left(\frac{\partial n_1}{\partial\omega}\right)_{\bar{\omega}_1}\right]\hat{\mathbf{k}}_1\right.\\ &\quad \left.-\left[\left(\frac{\partial^2 n_2}{\partial\omega^2}\right)_{\bar{\omega}_2}\bar{\omega}_2 + 2\left(\frac{\partial n_2}{\partial\omega}\right)_{\bar{\omega}_2}\right]\hat{\mathbf{k}}_2\right\}\frac{\delta\omega^2}{2},\end{aligned}$$

in which we suppose that the phase-matching condition is satisfied for the central frequencies of the interacting fields; that is,

$$\mathbf{k}_p(\omega_p) - \mathbf{k}_1(\bar{\omega}_1) - \mathbf{k}_2(\bar{\omega}_2) = 0. \quad (15)$$

Note that the terms of the first order in the squared brackets represent the group velocities as $v_g = c_0[(\partial n/\partial\omega)_{\bar{\omega}}\bar{\omega} + n(\bar{\omega})]^{-1}$, while those of the second order are dispersion terms. If we use the result in Eq. (14) to derive the scalar products appearing in Eq. (13), we obtain

$$\begin{aligned}\Delta\mathbf{k}\cdot\hat{\mathbf{k}}_1 &= \frac{1}{c}\left(-\left[\left(\frac{\partial n_1}{\partial\omega}\right)_{\bar{\omega}_1}\bar{\omega}_1 + n_1(\bar{\omega}_1)\right]\right.\\ &\left.+\left[\left(\frac{\partial n_2}{\partial\omega}\right)_{\bar{\omega}_2}\bar{\omega}_2 + n_2(\bar{\omega}_2)\right]\cos(\vartheta_1-\vartheta_2)\right)\delta\omega = \alpha_1\delta\omega, \quad (16a)\\ \Delta\mathbf{k}\cdot\hat{\mathbf{k}}_2 &= \frac{1}{c}\left(-\left[\left(\frac{\partial n_1}{\partial\omega}\right)_{\bar{\omega}_1}\bar{\omega}_1 + n_1(\bar{\omega}_1)\right]\cos(\vartheta_1-\vartheta_2)\right.\\ &\left.+\left[\left(\frac{\partial n_2}{\partial\omega}\right)_{\bar{\omega}_2}\bar{\omega}_2 + n_2(\bar{\omega}_2)\right]\right)\delta\omega = \alpha_2\delta\omega, \quad (16b)\end{aligned}$$

in which we have taken into account the terms up to first order in $\delta\omega$.

If we suppose that the approximation $4|A_p|^2/[(\Delta\mathbf{k}\cdot\hat{\mathbf{k}}_1)(\Delta\mathbf{k}\cdot\hat{\mathbf{k}}_2)] \gg 1$ holds and consider the relations in Eqs. (16), Eq. (13) can be written as

$$\begin{aligned}\Gamma &= \frac{\Delta\mathbf{k}\cdot\hat{\mathbf{k}}_2}{\Delta\mathbf{k}\cdot\hat{\mathbf{k}}_1}\sinh^2\left[\frac{2|A_p(0)|}{\sqrt{(\Delta\mathbf{k}\cdot\hat{\mathbf{k}}_1)(\Delta\mathbf{k}\cdot\hat{\mathbf{k}}_2)}}\right.\\ &\left.\times\left(1-\frac{1}{2}\frac{(\Delta\mathbf{k}\cdot\hat{\mathbf{k}}_1)(\Delta\mathbf{k}\cdot\hat{\mathbf{k}}_2)}{4|A_p(0)|^2}(\Delta\mathbf{k}\cdot\hat{\mathbf{k}}_1)\frac{L}{2}\right)\right]\\ &= \frac{\Delta\mathbf{k}\cdot\hat{\mathbf{k}}_2}{\Delta\mathbf{k}\cdot\hat{\mathbf{k}}_1}\frac{1}{4}\exp\left[2|A_p(0)|L\sqrt{\frac{\Delta\mathbf{k}\cdot\hat{\mathbf{k}}_1}{\Delta\mathbf{k}\cdot\hat{\mathbf{k}}_2}}\right.\\ &\left.\times\left(1-\frac{1}{2}\frac{(\Delta\mathbf{k}\cdot\hat{\mathbf{k}}_1)(\Delta\mathbf{k}\cdot\hat{\mathbf{k}}_2)}{4|A_p(0)|^2}\right)\right] \quad (17)\\ &\simeq \frac{\alpha_2}{\alpha_1}\frac{1}{4}\exp\left[2|A_p(0)|L\sqrt{\frac{\alpha_1}{\alpha_2}}\left(1-\frac{1}{2}\frac{\alpha_1\alpha_2\delta\omega^2}{4|A_p(0)|^2}\right)\right]\\ &= \frac{\alpha_2}{\alpha_1}\frac{1}{4}\exp\left[2|A_p(0)|L\sqrt{\frac{\alpha_1}{\alpha_2}}\right]\exp\left[-\frac{\alpha_1\sqrt{\alpha_1\alpha_2}}{4|A_p(0)|}L\delta\omega^2\right].\end{aligned}$$

From this expression, we can derive the full width at half maximum (FWHM) value of $\delta\omega$ corresponding to an amplification gain of $\Gamma = \Gamma_{\Delta k=0}/2$, being the first exponential on the last line of Eq. (17) the gain in perfect phase matching, i.e.,

$$\Delta\omega_{\mathrm{FWHM}} = 2\sqrt{\frac{4|A_p|\ln 2}{L\alpha_1\sqrt{\alpha_1\alpha_2}}}. \quad (18)$$

The knowledge of the width at half maximum of the amplified band allows us to calculate the number of

modes generated by the nonlinear interaction [4]. By assuming transform-limited pulses for which

$$\Delta t_{(\mathrm{FWHM})}\Delta\omega_{(\mathrm{FWHM})} = 8\ln 2, \tag{19}$$

we can define

$$\mu = \frac{\Delta\tau_p}{\Delta\tau_{(\mathrm{FWHM})}} = \Delta\tau_p\frac{\Delta\omega_{(\mathrm{FWHM})}}{8\ln 2}, \tag{20}$$

where $\Delta\tau_p$ is the time duration of the pump pulse centered at frequency ω_p. By substituting Eq. (18) into Eq. (20), we obtain an expression depending on the crystal parameters and on the intensity of the pump. Note that the number of the modes can also be calculated in the case of cw pumping, in which $\Delta\tau_p$ would be a characteristic time of the measurements, such as the duration of the observation time.

In Fig. 2, we plot the number of modes as a function of the frequencies of signal and idler evaluated as fractions of the frequency of the pump field at different pump intensities. In particular, we can notice that the number of modes grows both for larger values of the pump intensity and for frequencies closer to degeneracy, i.e., when signal and idler have the same frequency. In addition, when we are far from degeneracy, the dependence on the intensity of the pump is weaker.

2.1.2. Phase mismatching in direction. Here, we consider the phase-mismatching condition for small deviations in the direction of the wave vectors involved in the interaction. Even in this case, we are looking for an amplification that is halved with respect to that in perfect noncollinear phase matching. If we suppose that $\delta\vartheta_1$ is the angular deviation from the phase-matching condition in which the angle between the vectors $\mathbf{k}_1$ and $\mathbf{k}_p$ is given by $(\vartheta_p - \bar{\vartheta}_1)$, while $\delta\vartheta_2$ is the angular deviation for the vectors $\mathbf{k}_2$ and $\mathbf{k}_p$, we can derive the following expressions:

$$\mathbf{k}_p\cdot\mathbf{k}_1 \simeq k_p k_1[\cos(\vartheta_p - \bar{\vartheta}_1) + \sin(\vartheta_p - \bar{\vartheta}_1)\delta\vartheta_1], \tag{21a}$$

$$\mathbf{k}_p\cdot\mathbf{k}_2 \simeq k_p k_2[\cos(\vartheta_p - \bar{\vartheta}_2) + \sin(\vartheta_p - \bar{\vartheta}_2)\delta\vartheta_2], \tag{21b}$$

$$\begin{aligned}\mathbf{k}_2\cdot\mathbf{k}_1 \simeq k_1 k_2[&\cos(\bar{\vartheta}_2 - \bar{\vartheta}_1)\\ &+ \sin(\bar{\vartheta}_2 - \bar{\vartheta}_1)(\delta\vartheta_1 - \delta\vartheta_2)].\end{aligned} \tag{21c}$$

By substituting these expressions in the relation $(\Delta\mathbf{k}\cdot\mathbf{k}_2)/k_2 = (\Delta\mathbf{k}\cdot\mathbf{k}_1)/k_1$, which represents the condition to be fulfilled in order to match the solution in phase mismatch with that in perfect phase matching, it is possible to derive the relation between the angular deviations $\delta\vartheta_1$ and $\delta\vartheta_2$. By means of trigonometric considerations, we can simplify this relation as follows:

$$\begin{aligned}\delta\vartheta_1 &= \delta\vartheta_2\frac{k_p\sin(\vartheta_p - \bar{\vartheta}_2) + (k_1 - k_2)\sin(\bar{\vartheta}_2 - \bar{\vartheta}_1)}{k_p\sin(\vartheta_p - \bar{\vartheta}_1) + (k_1 - k_2)\sin(\bar{\vartheta}_2 - \bar{\vartheta}_1)}\\ &= -\delta\vartheta_2\frac{k_2}{k_1}.\end{aligned} \tag{22}$$

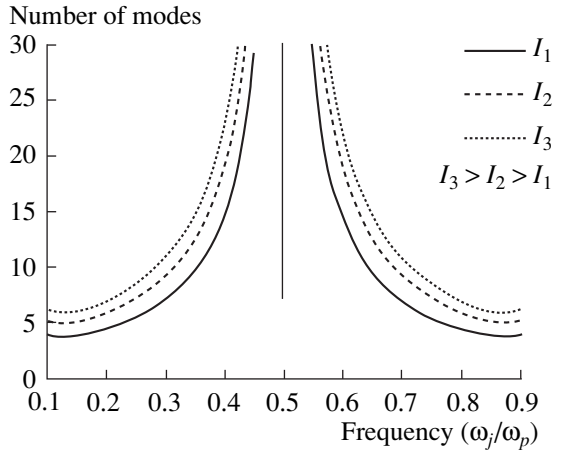

Fig. 2. Number of modes as a function of the frequencies of signal and idler (as fractions of the frequency of the pump field) and as a function of the intensity of the pump ($I_3 > I_2 > I_1$).

In order to derive the expression of the angular deviations corresponding to an amplification that is halved with respect to that in perfect noncollinear phase matching, we consider Eq. (13) and follow the same procedure as in the previous section, thus obtaining

$$\begin{aligned}\Gamma &= \frac{\Delta\mathbf{k}\cdot\hat{\mathbf{k}}_2}{\Delta\mathbf{k}\cdot\hat{\mathbf{k}}_1}\sinh^2\left[|A_p(0)|L\sqrt{\frac{(\Delta\mathbf{k}\cdot\hat{\mathbf{k}}_1)}{(\Delta\mathbf{k}\cdot\hat{\mathbf{k}}_2)}}\right.\\ &\left.\times\left(1 - \frac{1}{2}\frac{(\Delta\mathbf{k}\cdot\hat{\mathbf{k}}_1)(\Delta\mathbf{k}\cdot\hat{\mathbf{k}}_2)}{4|A_p(0)|^2}\right)\right]\\ &= \frac{1}{4}\exp\left[2|A_p(0)|L\left(1 - \frac{1}{2}\frac{(\Delta\mathbf{k}\cdot\hat{\mathbf{k}}_2)^2}{4|A_p(0)|^2}\right)\right]\end{aligned} \tag{23}$$

$$\begin{aligned}&\simeq \frac{1}{4}\exp\left[2|A_p(0)|L\left(1 - \frac{1}{2}\frac{(k_1\sin(\bar{\vartheta}_2 - \bar{\vartheta}_1)\delta\vartheta_1)^2}{4|A_p(0)|^2}\right)\right]\\ &= \frac{1}{4}\exp[2|A_p(0)|L]\exp\left[-\frac{Lk_1^2\sin^2(\bar{\vartheta}_2 - \bar{\vartheta}_1)}{4|A_p(0)|}\delta^2\vartheta_1\right],\end{aligned}$$

where we have again used the equality $(\Delta\mathbf{k}\cdot\hat{\mathbf{k}}_2) = (\Delta\mathbf{k}\cdot\hat{\mathbf{k}}_1)$ and Eq. (22).

Then, the FWHM angular deviation is

$$\delta\vartheta_{1,\,\mathrm{FWHM}} = 2\sqrt{\frac{4|A_p(0)|\ln 2}{L}\frac{1}{k_1^2\sin^2(\bar{\vartheta}_2 - \bar{\vartheta}_1)}}. \tag{24}$$

This analysis shows that spatial coherence areas exist in which the signal is amplified. We also notice that all the calculations have been developed by considering angular deviations in the plane (y, z) (see Fig. 1). If we extend this analysis to the third direction, we obtain a

surprising result: in fact, the spatial coherence areas are not circular, even if those that are near the principal plane can be considered as circles with a good approximation.

2.2. Quantum Evolution

Let us now analyze the interaction among the three modes taking into account quantum fluctuations. As in the classical case, we denote by a_1 the signal, a_2 the idler, and a_p the pump. The modes whose frequencies are linked by the relation $\omega_p = \omega_1 + \omega_2$ are coupled by the medium nonlinearity. In the rotating-wave approximation and under phase-matching conditions, the Hamiltonian can be written as follows:

$$H_1 \propto a_1 a_2 a_p^\dagger + a_1^\dagger a_2^\dagger a_p. \quad (25)$$

The interaction described by Hamiltonian (25) covers a considerably rich variety of phenomena, such as generation of correlated photon pairs by parametric downconversion [11–13], phase-insensitive amplification [6, 19], and realization of Bell states [13, 16, 17]. The unitary evolution operator in the interaction picture is

$$U_\tau = \exp[-i\tau(a_1 a_2 a_p^\dagger + a_1^\dagger a_2^\dagger a_p)], \quad (26)$$

where τ represents a rescaled interaction time. The parametric approximation consists of replacing the pump mode a_p with the complex amplitude γ of the corresponding coherent state, thus achieving the two-mode squeezing operator

$$U_\lambda = \exp[\lambda a_1^\dagger a_2^\dagger - \lambda^* a_1 a_2], \quad (27)$$

where the coupling λ is given by $\lambda = -i\tau\gamma$. Notice that the parametric approximation is valid for a wide range of values of the pump power, including also the case of a weak pump with small mean photon number. As a matter fact, the relevant parameter for the validity of the parametric approximation is the residual degree of coherence of the pump rather than its depletion [20].

The two-mode squeezing operator yields a suppression of the quantum fluctuations in one quadrature of the sum and difference of modes $a_1 \pm a_2$ [25]. Let us consider two coherent beams at the input of the system $|\psi_0\rangle = |\alpha_1\rangle_1|\alpha_2\rangle_2 = D_1(\alpha_1) \otimes D_2(\alpha_2)|\mathbf{0}\rangle$, where $D(\alpha) = \exp[\alpha a^\dagger - \alpha^* a]$ denotes the displacement operator and $|\mathbf{0}\rangle$ denotes the e.m. vacuum. The output state is given by (we neglect an overall phase)

$$|\psi_1\rangle = D_1(\mu\alpha_1 + \nu\alpha_2^*) \otimes D_2(\mu\alpha_2 + \nu\alpha_1^*)|\psi_{\text{twb}}\rangle, \quad (28)$$

where $\mu = \cosh|\lambda|$, $\nu = \sinh|\lambda|$ (we assume, without loss of generality, a real pump amplitude γ) and $|\psi_{\text{twb}}\rangle$ denotes the so-called twin beam (TWB)

$$|\psi_{\text{twb}}\rangle = U_\lambda|\mathbf{0}\rangle = \sqrt{1-|\chi|^2}\sum_{n=0}^{\infty}\chi^n|n\rangle_1 \otimes |n\rangle_2, \quad (29)$$

which represents the maximally entangled state of the two modes a_1 and a_2 (see below). The expression in Eq. (29), with $\chi = \arg(\lambda)\tanh|\lambda|$, can be easily derived by factorizing U_λ through the decomposition formulas for the $SU(1, 1)$ Lie algebra [6, 21, 22], i.e.,

$$\begin{aligned}\exp[\lambda a_1^\dagger a_2^\dagger - \lambda^* a_1 a_2] &= \exp\left[a_1^\dagger a_2^\dagger \frac{\lambda}{|\lambda|}\tanh\lambda\right] \\ &\times \exp[-\log(\cosh^2\lambda)(a_1^\dagger a_1 + a_2^\dagger a_2 + 1)] \\ &\times \exp\left[-a_1 a_2 \frac{\lambda^*}{|\lambda|}\tanh\lambda\right].\end{aligned} \quad (30)$$

The mode transformations are given by

$$U_\lambda^\dagger \begin{pmatrix} a_1 \\ a_2 \end{pmatrix} U_\lambda = \begin{pmatrix} \mu a_1 - \nu a_2^\dagger \\ -\nu a_1^\dagger + \mu a_2 \end{pmatrix}. \quad (31)$$

The gain of the device can be defined by taking, as the initial condition, either the signal or the idler modes excited in some arbitrary state, and the other mode in the vacuum. By using Eq. (31), we arrive at the expression

$$G_j = \frac{\langle a_j^\dagger a_j\rangle_o - \langle a_j^\dagger a_j\rangle_i}{\langle a_j^\dagger a_j\rangle_i} = \sinh^2|\lambda|\left(1 + \frac{1}{\langle a_j^\dagger a_j\rangle_i}\right), \quad (32)$$

where $\langle\ldots\rangle_{i,o}$ denote the expectation value at the input and the output, respectively. The first term in Eq. (32) coincides with the analogous quantity defined in the classical analysis of the parametric amplifier. On the other hand, the second term corresponds to the parametric downconversion from the vacuum (usually also referred to as parametric spontaneous emission), namely, a genuine quantum effect. Indeed, the total number of photons carried by the twin beam of Eq. (29) is given by

$$\langle\psi_{\text{twb}}|a_1^\dagger a_1 + a_2^\dagger a_2|\psi_{\text{twb}}\rangle = 2\sinh^2|\lambda|. \quad (33)$$

The TWB, as well as the state generated by downconversion from a coherent seed or a thermal background, are Gaussian states, i.e., are described by a Wigner function of the form [30]

$$W[\varrho](\mathbf{X}) = \left(\frac{2}{\pi}\right)^2 \frac{1}{\sqrt{\det[\boldsymbol{\sigma}]}} e^{-\frac{1}{2}(\mathbf{X}-\bar{\mathbf{X}})^T\boldsymbol{\sigma}^{-1}(\mathbf{X}-\bar{\mathbf{X}})}, \quad (34)$$

where $\mathbf{X} = (x_1, y_1, x_2, y_2)$ is the Cartesian description of the phase space of two modes. The covariance matrix $\boldsymbol{\sigma}$ is defined as

$$\sigma_{kl} \equiv [\boldsymbol{\sigma}]_{kl} = \frac{1}{2}\langle\{R_k, R_l\}\rangle - \langle R_l\rangle\langle R_k\rangle, \quad (35)$$

where $\mathbf{R} = (q_1, p_1, q_2, p_2)^T$ is the vector of the quadratures of the two modes, i.e.,

$$q_k = \frac{1}{\sqrt{2}}(a_k + a_k^\dagger), \quad p_k = \frac{i}{\sqrt{2}}(a_k^\dagger - a_k), \tag{36}$$

in which $\{A, B\} = AB + BA$ denotes the anticommutator and $\langle O \rangle \equiv \bar{O} = \mathrm{Tr}[\varrho O]$ is the expectation value of the operator O, where ϱ is the density matrix of the system. The mean values of the field are given by $\bar{X}_k = \langle R_k \rangle$, whereas the canonical commutation relations are rewritten as

$$[R_k, R_l] = \frac{i}{2\kappa_1^2}\Omega_{kl}, \tag{37}$$

where Ω_{kl} are the elements of the symplectic matrix

$$\mathbf{\Omega} = \bigoplus_{k=1}^{2} \boldsymbol{\omega}, \quad \boldsymbol{\omega} = \begin{pmatrix} 0 & 1 \\ -1 & 0 \end{pmatrix}. \tag{38}$$

Uncertainty relations among canonical operators impose a constraint on the covariance matrix, corresponding to the inequalities [31]

$$\boldsymbol{\sigma} + \frac{i}{2}\mathbf{\Omega} \geq 0. \tag{39}$$

Equations (39) follow from the uncertainty relations for the mode operators and express, in a compact form, the positivity of the density matrix ϱ.

For bipartite and tripartite Gaussian states, the positivity of the partial transpose (PPT) of the density matrix is a necessary and sufficient condition for separability. In turn, the PPT condition may be written in terms of the covariance matrix [32]

$$\boldsymbol{\sigma} + \frac{i}{2}\tilde{\mathbf{\Omega}} \geq 0, \tag{40}$$

where $\tilde{\mathbf{\Omega}} = \mathbf{\Lambda}\mathbf{\Omega}\mathbf{\Lambda}$ denote the modified symplectic matrix, $\mathbf{\Lambda} = \mathrm{Diag}(1, 1, 1, -1)$ being the matrix describing the partial transposition in the phase space (time reversal for one of the modes). For TWB and the displaced TWB of Eq. (28), the covariance matrix reads

$$\boldsymbol{\sigma}_{\mathrm{TWB}} = \frac{1}{2}\begin{pmatrix} \cosh(2r)1_2 & \sinh(2r)\boldsymbol{\sigma}_3 \\ \sinh(2r)\boldsymbol{\sigma}_3 & \cosh(2r)1_2 \end{pmatrix}, \tag{41}$$

where $\boldsymbol{\sigma}_3 = \mathrm{Diag}(1, -1)$ is a Pauli matrix and $r = |\lambda|$. For TWB, inequality (40) is violated for any value of λ; i.e., TWB are entangled states (actually, TWB are maximally entangled states; i.e., the violation is maximal for a fixed number of photons). If the interaction described by U_λ starts from a thermal background rather than from the vacuum or from coherent signals, then the covariance matrix is modified, and, using Eq. (40), one can show that the corresponding state is entangled only if the coupling constant λ exceeds a threshold value [30].

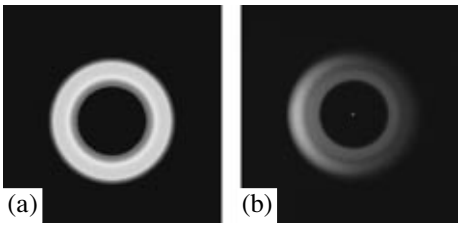

Fig. 3. (a) Simulated image of the SPDC cones with the tuning angle $\alpha = 34.25°$; (b) picture of the SPDC cones with the tuning angle $\alpha = 34.25°$.

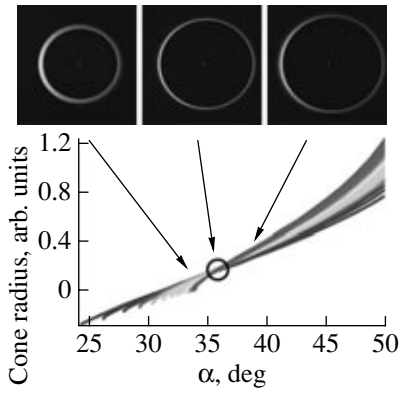

Fig. 4. Upper panel: pictures of the SPDC cones before the inversion zone (on the left), in the inversion zone (in the center), and after the inversion zone (on the right). Lower panel: radii of the signal cones as functions of the tuning angle. For $\alpha = 35.9°$, there is the superposition zone, after which the frequencies invert their positions.

2.3. Applications: TWB State Generation

If an intense pump field at frequency ω_p enters a second-order nonlinear crystal, it generates both the signal and the idler fields at frequencies ω_1 and ω_2, with $\omega_p = \omega_1 + \omega_2$. The process, well known as spontaneous parametric downconversion (SPDC), involves all the wave vectors that, together with the frequency-matching condition, satisfy the phase-matching condition, i.e., $\Delta k = 0$. In uniaxial crystals, the SPDC consists of the generation of concentric broadly tunable cones [33], whose frequencies depend on that of the pump field and whose apertures depend on the tuning angle. Figure 3a shows the calculated signal cones at the exit of the crystal for a fixed value of the tuning angle ($\alpha = 34.25°$) and of the wavelength of the pump field ($\lambda_p = 349$ nm). The experimental counterpart of this simulation is shown in Fig. 3b, which is a picture taken with a digital camera (Coolpix 990, Nikon, Japan).

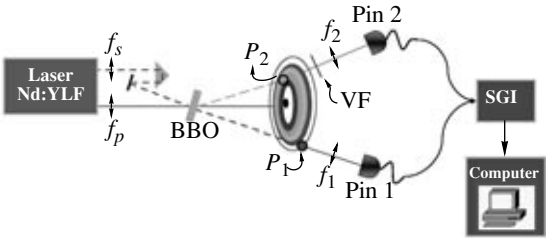

Fig. 5. Experimental setup for measurements on the TWB: BBO, nonlinear crystal; $P_{1,\,2}$, pinholes; $f_{p,\,s,\,1,\,2}$, lenses; Pin 1, 2, *p–i–n* photodiodes; SGI, synchronous gated integrator.

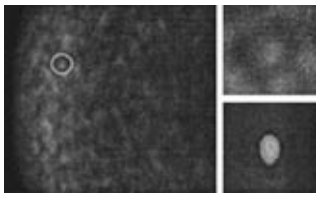

Fig. 6. Left: single-shot picture of a portion of the signal cone. Right, top: magnification of a single coherence area around λ_2. Right, bottom: intensity map of a typical coherence area used to estimate its dimensions.

It is also interesting to notice that, as α grows, more and more frequencies appear in the cones. Moreover, for $\alpha = 35.9°$, we observe the so-called *inversion zone* in which all the frequencies are superimposed (see Fig. 4, lower panel). Indeed, for greater values of α, we can observe that the cones corresponding to the lower frequencies are outside those relative to the higher frequencies (for example, the red cone is outside the green one). This behavior is shown in detail in the upper panel of Fig. 4, in which there are three pictures of the cones before the inversion zone, in correspondence of it and after it.

To produce the SPDC, we pumped a nonlinear crystal with the frequency-tripled pulses emitted by a continuous-wave mode-locked Nd:YLF laser regeneratively amplified at a repetition rate of 500 Hz (High Q Laser Production, Austria). The laser delivers ~7.7-ps pulses at the fundamental frequency. The crystal was an uncoated β-BaB_2O_4 crystal (BBO, Fujian Castech Crystals, Fuzhou, China) cut for type-I interaction ($\vartheta_{CUT} = 34°$), having a cross-section of 10×10 mm and a thickness of 4 mm (see Fig. 5) [34]. The pump beam, which emerges from the laser slightly divergent, was focused by lens f_p of focal length 500 mm. The crystal tuning angle was 33.1°; the visible portion of the cones projected on a screen beyond the BBO is shown in Fig. 5. We operated the system in a dichromatic configuration by choosing the frequency of the laser second harmonics ($\lambda_2 = 523$ nm) for the signal and, consequently, the frequency of the laser fundamental ($\lambda_1 = 1047$ nm) for the idler. For alignment purposes, a portion of the fundamental beam emerging from the laser was collimated (by a lens of focal length $f_s = 1000$ mm) and sent to the crystal together with the pump beam so as to obtain a well-recognizable spot of amplified seeded downconversion.

As explained in Subsection 2.1.2, the mismatching in direction is responsible for the existence of spatial coherence areas in which the amplification of the process holds. The components of a TWB state have a spatial divergence that depends on the pump field intensity (see Eq. (24)) and that are related to each other according to Eq. (22). In Fig. 6 (left), we show the single-shot picture of a portion of the signal cone taken with the digital camera, in which we can clearly distinguish the presence of the coherence areas. In the right part (top) of the same figure, one can see a magnified single coherence area around λ_2 (green light) and (bottom) the intensity map of a typical coherence area taken with a CCD camera (TM-6CN, Pulnix, United Kingdom; operated at high resolution).

To spatially select the components of the twin beam at the wavelengths 1047 and 523 nm, we used two pinholes, P_1 and P_2, located on the outputs of the seeded process. Their dimensions were determined by studying the size of single-shot coherence areas as functions of the pump power and of the distance from the crystal. In particular, to realize a compact setup, we decided to place at the same distance (72.5 cm from the BBO) two pinholes having different dimensions (diameter $\simeq$3.5 mm on the signal and $\simeq$7 mm on the idler). The light selected by the pinholes and filtered was then focused by two lenses (f_1 and f_2, with focal length 25 mm) on two *p–i–n* photodiodes (85973-02, Hamamatsu, Japan: 1-ns time response, 500-μm-diameter sensitive area on the green; and G8376-05, Hamamatsu, Japan: 5-ns time response, 500-μm-diameter sensitive area on the IR) having nominal quantum efficiencies of $\eta_1 = 0.78$ and $\eta_2 = 0.92$, respectively. Each current output was integrated over a synchronous gate of suitable time duration (40 ns) by a synchronous gated integrator (SGI) in external trigger modality; each SGI output was then digitized by a 13-bit converter (SR250, Stanford Research Systems, with 50-mV full scale), and the counts were stored in a PC-based multichannel analyzer.

The measurements were performed by inserting a variable filter (VF in Fig. 5) in front of the photodiode that detects the signal and by carefully adjusting it to balance the quantum efficiencies of the detection branches of the setup. Thus, the overall quantum efficiency of the apparatus turned out to be $\eta_{1tot} \simeq \eta_{2tot} = 0.67$.

2.4. Experimental Results

First, we verified the linearity of the gated integrators and measured the conversion coefficients ($\alpha_1 =$

6.7182×10^{-8} V and $\alpha_2 = 8.3043 \times 10^{-8}$ V) by linking each output voltage to the number of electrons forming the photocurrent output pulse of the detector at each laser shot. The relations among the statistical distributions of the number of photons incident on the detector, $p_{ph}(n)$, that of the number of detected photons, $p_{el}(m)$, and that of the output voltages, $p_{out}(v)$, are given by

$$p_{el}(m) = \sum_{n=m}^{\infty} \binom{n}{m} \eta^m (1-\eta)^{n-m} p_{ph}(n), \quad (42)$$

$$p_{out}(v) = C p_{el}(\alpha m), \quad (43)$$

where α is the measured conversion coefficient mentioned above and C is a normalization coefficient. If we limit our analysis to the first two momenta of the distributions, we obtain the following relations between the different quantities:

$$V = \alpha M = \alpha \eta N, \quad (44)$$

$$\sigma_{out}^2(v) = \alpha^2 \sigma_{el}^2(m) = \alpha^2 [\eta^2 \sigma_{ph}^2(n) + \eta(1-\eta)N], \quad (45)$$

where V is the output voltage of the digitizer, M is the total photoelectron number, and N is the total photon number. Note that, in general, the statistical distribution for the measured outputs is different from that of the incident photons. As we will see below, in our measurements, the statistical distributions of the detected photons and that of the voltage outputs are multithermal, with the duration of the pump longer than the coherence time (see Eq. (20)). However, if the mean photon number is large enough, in the expression for the variance of the detected photons

$$\sigma^2(m) = \eta^2 \frac{\langle N \rangle^2}{\mu} + \eta(1-\eta)\langle N \rangle, \quad (46)$$

in which μ is the number of temporal modes, we can neglect the second term, and the dependence of the photoelectron statistics on that of the photons is simply linear.

In Figs. 7a and 7b, we show the recorded signal and idler outputs of the photodiodes for the same sequence of pump-laser shots, together with the noise of the detectors. We notice that the variance of the output voltage corresponding to the measurements performed in the presence of the TWB is greater than that relative to the noise measurements, since the statistics of signal and idler are multithermal. Moreover, the corresponding normalized probability distributions reported in Figs. 8a and 8b for the same data are well fitted by multithermal distributions [33], i.e., those obtained by the convolution of μ equally populated thermal modes

$$p_{out,\mu}(v) = \frac{\exp(-v\mu/V_T)}{(\mu-1)!} \frac{v^{\mu-1}}{(V_T/\mu)^{\mu}}, \quad (47)$$

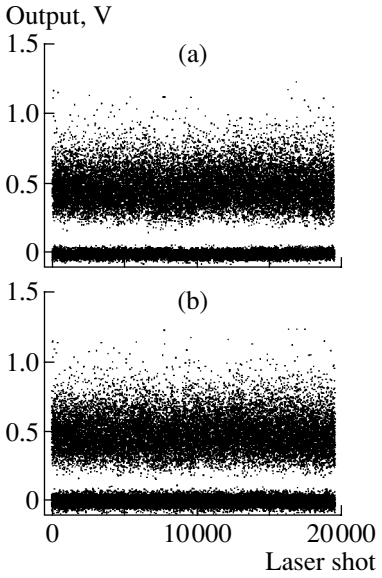

Fig. 7. (a) Output voltages for the signal beam at $\lambda_2 = 523$ nm for a sequence of laser shots and of dark measurements; (b) output voltages for the idler beam at $\lambda_1 = 1047$ nm for the same sequence of laser shots and of dark measurements.

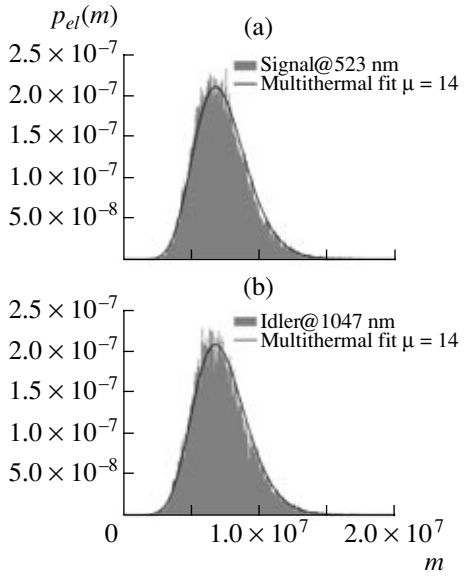

Fig. 8. (a) Histogram of the photoelectron distribution of the signal beam output at $\lambda_2 = 523$ nm together with the corresponding multithermal fit. The conversion coefficient that links the voltage output of the digitizer to the number of electrons forming the photocurrent output pulse of the detector at each laser shot is $\alpha_2 = 8.3043 \times 10^{-8}$ V. (b) Histogram of the photoelectron distribution of the idler beam output at $\lambda_1 = 1047$ nm together with the corresponding multithermal fit. The conversion coefficient that links the voltage output of the digitizer to the number of electrons forming the photocurrent output pulse of the detector at each laser shot is $\alpha_1 = 6.7182 \times 10^{-8}$ V.

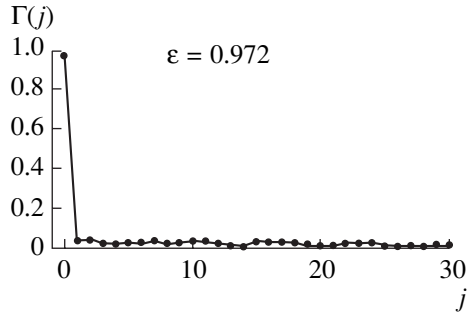

Fig. 9. Correlation function between signal and idler beams as a function of the delay in the laser shots.

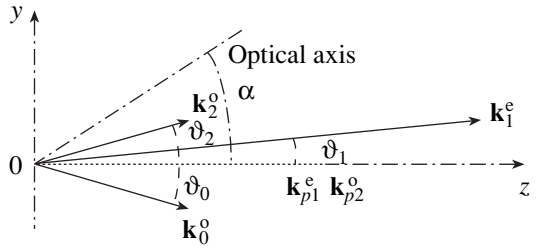

Fig. 10. Scheme of the interaction inside the crystal, with y oriented along the entrance face of the crystal. ϑ_j are the internal phase-matching angles, α is the tuning angle, and $\mathbf{k}_j^{o,e}$ are the wave vectors of the interacting fields.

where $V_T = \alpha M_T$ is the mean output corresponding to the mean value M_T of overall detected photons. Equation (47) holds in the high-intensity regime, which is the present experimental condition. In fact, by using the measured conversion coefficients on the detection arms of signal and idler, we obtained $M_1 = 7.225 \times 10^6$ and $M_2 = 7.212 \times 10^6$ as the mean number of detected photons. As it is well known from the theory of photodetection [4], the number of detected modes can be interpreted as the ratio of the time characteristic of the measurement (in our case, the time duration of the pulse) and the coherence time characteristic of the field to be measured (in our case, the inverse of the temporal bandwidth of the spontaneous parametric downconversion) [33]. The continuous lines superimposed to the histograms of the experimental data in Figs. 8a and 8b show the convolution integrals, optimized for the number of temporal modes, of the theoretical distribution in Eq. (47) with the system impulse response evaluated from measurements performed in the absence of incident light. As expected, the signal and idler distributions are well fitted by multithermal distributions having the same number of modes ($\mu = 14$). Note that the probability distributions for signal and idler are very similar to each other. In order to quantify the correlation, we use the function [4]

$$\Gamma(j) = \frac{\langle (I_1(k) - \langle I_1 \rangle)(I_2(k+j) - \langle I_2 \rangle) \rangle}{\sigma(I_1)\sigma(I_2)}, \quad (48)$$

where $\langle \ldots \rangle$ denotes the average over the complete set of data; $I_j(k)$ is the number of detected photons $j = 1, 2$ for the kth shot; and $\sigma(I_j) = \sqrt{\langle I_j^2 \rangle - \langle I_j \rangle^2} = \sqrt{\eta_j^2 \sigma_{\hat{n}_j}^2 + \eta_j(1-\eta_j)\langle \hat{n}_j \rangle}$ is the corresponding rms, where $\hat{n}_j = c_j^\dagger c_j$ and η_j is the quantum efficiency. In particular, $\varepsilon = \Gamma(0)$ is the correlation coefficient

$$\varepsilon = \frac{\langle I_1 I_2 \rangle - \langle I_1 \rangle \langle I_2 \rangle}{\sigma(I_1)\sigma(I_2)}. \quad (49)$$

Note that, in the case of a multithermal statistics, the correlation coefficient for the TWB state reads as follows:

$$\varepsilon_{TWB} = \sqrt{\frac{(\sqrt{(M_1/\mu)(M_2/\mu)} + \sqrt{\eta_1 \eta_2})^2}{(M_1/\mu + 1)(M_2/\mu + 1)}}, \quad (50)$$

which, in the limit of intense fields, tends to 1 for any value of η_j. In Fig. 9, we show the correlation function for the data of Figs. 7a and 7b: the contribution of the noise of the apparatus has been subtracted from the measured variances of the experimental data. We obtained $\varepsilon = 0.97$, to be compared with a theoretical value of about 1. Note that subsequent shots result to be uncorrelated.

3. FIVE-MODE PARAMETRIC PROCESSES

In this section, we analyze the parametric interaction taking place among five modes of the field in a single crystal in suitable phase matching. First, we derive the classical equations of motion and solve them within the parametric approximation. We theoretically show, and experimentally demonstrate, that, for a single signal at the crystal input, two holographic replicas are obtained at the output. In addition, the implementation of several kinds of all-optical logical gates is analyzed. Then, the generation of three-mode entanglement is discussed in detail, and its application to $1 \longrightarrow 2$ telecloning is described. Finally, the experimental realization of five-wave interactions is demonstrated, and the results for the photon correlations are reported.

3.1. Classical Evolution

A scheme to realize multiple nonlinear processes is represented by two interlinked $\chi^{(2)}$ interactions occurring in a single crystal in type-I noncollinear phase-matching geometry. In this system, the choice of noncollinear phase matching provides remarkable flexibility to our experimental setup.

The process involves five fields a_j that are frequency-matched as follows: $\omega_{p1} = \omega_0 + \omega_2$, $\omega_1 = \omega_2 + \omega_{p2}$ (see Fig. 10). The fields, which propagate inside the crystal at angles ϑ_j with respect to the normal to the crystal entrance face, are chosen so as to allow the two interactions to be simultaneously phase-matched: $\mathbf{k}_{p1}^{e} = \mathbf{k}_0^{o} + \mathbf{k}_2^{o}$ and $\mathbf{k}_1^{e} = \mathbf{k}_2^{o} + \mathbf{k}_{p2}^{o}$, where $\mathbf{k}_j^{o,e}$ are the wave vectors in the medium, ordinary (o) and extraordinary (e), corresponding to frequencies ω_j.

We note that it is possible to satisfy these conditions with a number of different sets of frequencies and interaction angles depending on the choice of the nonlinear medium. In particular, to obtain a compact interaction geometry, we realized experiments in which $\omega_{p1} = \omega_{p2}$ and $\mathbf{k}_{p1}^{e} \parallel \mathbf{k}_{p2}^{o}$, thus implicitly neglecting walk-off in the crystal.

In general, the process is described by a set of five noncollinear equations; however, since the internal angles ϑ_j are quite small, the collinear approximation holds. Under this hypothesis, the complex field amplitudes a_j obey

$$da_0/dz = -ic_1 a_{p1} a_2^*, \tag{51a}$$

$$da_1/dz = -ic_2 a_{p2} a_2, \tag{51b}$$

$$da_2/dz = -ic_1 a_{p1} a_0^* - ic_2 a_{p2}^* a_1, \tag{51c}$$

$$da_{p1}/dz = -ic_1 a_0 a_2, \tag{51d}$$

$$da_{p2}/dz = -ic_2 a_2^* a_1, \tag{51e}$$

where c_1 and c_2 are coupling parameters

$$c_1 = \sqrt{\frac{2\hbar\omega_0\omega_2\omega_{p1}\eta_0^3}{n_0^o n_2^o n_{p1}^e}}[d_{22}\cos(\alpha - \vartheta_{p1}) + d_{31}\sin(\alpha - \vartheta_{p1})], \tag{52}$$

$$c_2 = \sqrt{\frac{2\hbar\omega_1\omega_2\omega_{p2}\eta_0^3}{n_1^e n_2^o n_{p2}^o}}[d_{22}\cos(\alpha - \vartheta_1) + d_{31}\sin(\alpha - \vartheta_1)], \tag{53}$$

where η_0 is the vacuum impedance, $n_j^{o,e}$ is the refractive index at ω_j, α is the tuning angle of the crystal, and d_{22} and d_{31} are the relevant elements of the $\chi^{(2)}$ tensor.

In order to obtain an analytical solution of Eqs. (51), it is also necessary to suppose that two of the interacting fields are nondepleted pump fields (parametric approximation), so that only the three remaining fields evolve as they propagate inside the crystal [40]. We note that any of the five interacting fields could be taken as undepleted pump, but, as for the experiments shown in the following, we considered a_{p1} and a_{p2} as the pumps, and we present the analytical solution for the other three fields, namely, a_0, a_1, and a_2:

$$a_0(z) = -\frac{1}{\Gamma^2}[|g_0|^2\cos(\Gamma z) - |g_1|^2]a_0(0) - \frac{g_0 g_1}{\Gamma^2}[\cos(\Gamma z) - 1]a_1^*(0) - i\frac{g_0}{\Gamma}\sin(\Gamma z)a_2^*(0), \tag{54a}$$

$$a_1(z) = \frac{g_0 g_1}{\Gamma^2}[\cos(\Gamma z) - 1]a_0^*(0) - \frac{1}{\Gamma^2}[|g_0|^2 - |g_1|^2\cos(\Gamma z)]a_1(0) - i\frac{g_1}{\Gamma}\sin(\Gamma z)a_2(0), \tag{54b}$$

$$a_2(z) = -i\frac{g_0}{\Gamma}\sin(\Gamma z)a_0^*(0) - i\frac{g_1^*}{\Gamma}\sin(\Gamma z)a_1(0) + \cos(\Gamma z)a_2(0), \tag{54c}$$

in which $g_0 = c_1 a_{p1}$, $g_1 = c_2 a_{p2}$, and $\Gamma = (|g_1|^2 - |g_0|^2)^{1/2}$.

3.2. Applications: Holography

The analytical solution in Eqs. (54) shows that each of the three evolving fields, namely, a_0, a_1, and a_2, depends on the others and on the pump fields. In this property, we directly recognize the holographic nature of the nonlinear process: generated fields are phase-conjugate with respect to $a_0(0)$, i.e., $a_1(z) \propto a_0^*(0)$ and $a_2(z) \propto a_0^*(0)$. We can thus consider the seed field as an object field at ω_0 and expect that the fields $a_1(z)$ and $a_2(z)$ reconstruct two real holographic images [28].

In order to verify this behavior, we constructed an experimental setup (see Fig. 11) in which the nonlinear medium was a type-I β-BaB_2O_4 crystal (BBO, cut angle 32°, cross-section 10 × 10 mm, and thickness 4 mm, Fujian Castech Crystals, Inc., Fuzhou, China), while the interacting fields were provided by the harmonics of a multimode Q-switched amplified Nd:YAG laser (7-ns pulse duration, Quanta-Ray GCR-4, Spectra-Physics, CA) at the wavelengths $\lambda_0 = \lambda_2 = 1064$ nm, $\lambda_1 = 355$ nm, and $\lambda_{p1} = \lambda_{p2} = 532$ nm. The pump fields at the wavelengths λ_{p1} and λ_{p2} were superimposed in a single beam with mixed polarization. In addition, to calculate the interaction angles, we assumed that the wave vectors $\mathbf{k}_{p1}$ and $\mathbf{k}_{p2}$ were normal to the crystal entrance face. To satisfy the phase-matching conditions, the other interacting fields must form with the normal the following internal angles: $\vartheta_0 = -\vartheta_2 = 10.6°$, $\vartheta_1 = 3.5°$, with a crystal tuning angle $\alpha = 37.74°$. Since our BBO crystal was cut at 32°, it had to be rotated to allow phase matching, with the only consequence of reducing the effective aperture of the crystal, which nevertheless remained wide enough to be considered as an infinite plane [29].

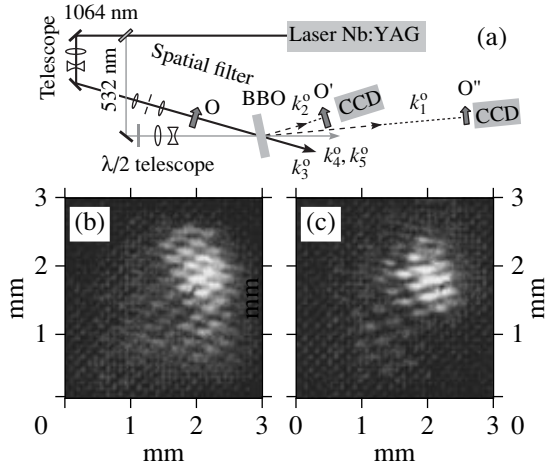

Fig. 11. (a) Experimental setup for the verification of the holographic properties of the generated fields. **O**, object; **O'** and **O"**, the reconstructed real holographic images at ω_2 and ω_1, respectively. (b) Holographic image at ω_2. (c) Holographic image at ω_1.

As the object **O**, we inserted a regular plastic net (80-μm-diameter wires spaced by 120 μm) on the beam at λ_0 at a distance of $d = 20$ cm from the BBO. In this way, the field diffracted by the net entirely covered the BBO crystal. In Figs. 11b and 11c, we show the holographic images of the net as detected by a CCD camera (PE2015, Pulnix, United Kingdom) along the direction of the output fields at λ_2 at a distance of 20.5 cm $\simeq d$ (Fig. 11b) and at λ_1 at a distance of 58 cm $\simeq 3d$ (Fig. 11c). The distances fit those expected [28], and the transversal dimensions are the same as those of the original object, again in very good agreement with theory [29].

3.3. Applications: All-Optical Logic Gates

The dependence of each of the evolving fields on the others and on the pump fields allows us to control the output fields by means of the input ones, and, for this reason, this scheme is suitable for the implementation of several kinds of all-optical devices, such as logic gates, looping circuits, and switches with an excellent optical resolution due to the holographic nature of the process [38].

In particular, the interlinked interactions allow the realization of all the logic functions of two variables, by encoding binary data inputs as amplitude modulation of the fields injected into the crystal. The outputs of the device, also being fields modulated in amplitude, carry data that can be read or reused as the inputs of another similar device.

Here, we present, both theoretically and experimentally, the possibility to use this scheme to produce, in a single type-I BBO crystal, the basic logic gates AND, OR, and NOT.

To do this, we calculate the squared amplitudes of the evolving fields for the initial conditions of interest.

As a first case, we consider the solution for field $a_1(z)$ in Eq. (54b) under the hypothesis of a crystal seeded only by field $a_0(0)$, while $a_1(0) = 0$ and $a_2(0) = 0$:

$$|a_1(z)|^2 = |g_0|^2|g_1|^2|a_0(0)|^2 \times \left[\frac{\cos^2(\sqrt{|g_1|^2 - |g_0|^2}z) - 2\cos(\sqrt{|g_1|^2 - |g_0|^2}z) + 1}{(|g_1|^2 - |g_0|^2)^2}\right]. \quad (55)$$

We note that the term within squared brackets is a multiplicative constant which is different from zero provided $|g_0|^2 \neq |g_1|^2$; so, apart from a scaling factor, the generation of field $a_1(z)$ only depends on the presence of the seed $a_0(0)$ and of the two pump fields through g_0 and g_1. This means that, for fixed values of $a_0(0)$, g_0, and g_1, $a_1(z)$ assumes the value expected from the theory [35], while, when one of the input field is absent, $a_1(0)$ vanishes.

From Eq. (55), we can deduce a boolean expression between binary numbers A_j corresponding to the squared amplitudes $|a_j|^2$, by setting $A_j = 1$ (with $j = 0$, $p1$, $p2$) if $|a_j(0)| \neq 0$ and $A_j = 0$ if $|a_j(0)| = 0$, that is, when the corresponding field is absent. Thus,

$$A_1 = A_0 \cdot A_{p1} \cdot A_{p2}, \quad (56)$$

where the symbol · represents the boolean operator AND. In this context, A_1, which corresponds to $|a_1(z)|^2$, also represents a binary number, having possible values equal to 0 or 1.

As a second case, we consider the solution for field $a_2(z)$ in Eq. (54c) with $a_2(0) = 0$ as the initial condition:

$$|a_2(z)|^2 = \{|g_0|^2|a_0(0)|^2 + |g_1|^2|a_1(0)|^2 + 2\mathrm{Re}[g_0^* g_1^* a_0(0)a_1(0)]\}\frac{\sin^2(\sqrt{|g_1|^2 - |g_0|^2}z)}{|g_1|^2 - |g_0|^2}. \quad (57)$$

The fraction on the right-hand side is a scaling factor, similarly to the previous case, while the term $2\mathrm{Re}[g_0^* g_1^* a_0(0)a_1(0)]$ is an interference contribution that becomes relevant only under strong conditions of phase stability and spatiotemporal superposition among the fields. Due to the multimode nature of our laser source, in our experimental setup, we could not achieve such conditions, and, thus, we can neglect the interference term and treat the two interactions seeded by $a_0(0)$ and $a_1(0)$ as independent.

By taking into account Eqs. (52) and (53), the boolean expression we can extract from Eq. (57) is

$$A_2 = A_0 \cdot A_{p1} + A_1 \cdot A_{p2}, \quad (58)$$

where the symbol + represents the boolean operator OR.

As a third case, we set $a_0(0) = 0$, $a_1(0) = 0$, and $g_0 = 0$ (i.e., $a_{p1}(0) = 0$), as the initial condition and obtain the following expression for the squared amplitude of $a_2(z)$:

$$|a_2(z)|^2 = \cos^2(|g_1|z)|a_2(0)|^2. \quad (59)$$

Equation (59) shows that, when the product $|g_1|z$ approaches $\pi/2$, field $a_2(z)$ becomes completely depleted by the interaction, while, when it exceeds $\pi/2$, the efficiency of the depletion is reduced again.

By associating the binary numbers A_2 and A_{p2} to the field amplitudes $|a_2(z)|^2$ and $|a_{p2}|^2$, respectively, Eq. (59) supplies the following boolean relation:

$$A_2 = \bar{A}_{p2}, \quad (60)$$

where the superscript "– " means the NOT operator.

Implementing the NOT gate is thus a task requiring that only one input be encoded as amplitude modulation on the pump field a_{p2}, whereas the seed field $a_2(0)$ should have a flat wave front.

We decided to realize the optical gates AND, OR, and NOT by encoding the data only on the pump fields a_{p1} and a_{p2}, to have all the inputs at the same wavelength. The other fields required by the interactions, $a_0(0)$ and $a_1(0)$, have a flat wave front and do not carry any logical data. Under these assumptions, Eqs. (56) and (58) reduce to

$$A_1 = A_{p1} \cdot A_{p2}, \quad (61a)$$

$$A_2 = A_{p1} + A_{p2}. \quad (61b)$$

For the implementation of these gates, we used the laser source just described above, and, in particular, we adopted the same interaction angles.

As depicted in Fig. 12, the harmonic outputs of the laser, which emerge in a single beam about 8 mm in diameter, were split into different directions by harmonic separators. The polarization of the second-harmonic field was projected along the ordinary and extraordinary axes by a thin-film plate polarizer in order to modulate the amplitudes of the two polarization components independently of each other. The two components then recombined in a second thin-film plate polarizer placed just before the BBO.

Typical energies of the input fields were $E_0 \sim 30$ mJ, $E_1 \sim 10$ mJ, $E_2 \sim 10$ mJ, $E_{p1} \sim 140$ mJ, and $E_{p2} \sim 115$ mJ (apart from the realization of the NOT gate in which $E_{p2} \sim 200$ mJ).

The binary numbers were encoded by using copper masks (~0.5 mm in thickness) having suitable holes (with a diameter of about 1 mm and an interspace of about 0.4 mm). Since we operated in positive logic, the transmission of light through the holes encoded the logic value 1. Each mask placed on fields a_{p1} and a_{p2} carried four bits, two equal to 0 and two equal to 1. For the implementation of the AND and OR gates, the mask on a_{p1} had two holes vertically aligned on the right part of the beam, while the mask on a_{p2} had two holes horizontally aligned in the top part of the beam. For the NOT gate, we used only one mask placed on a_{p2} with the two holes vertically aligned.

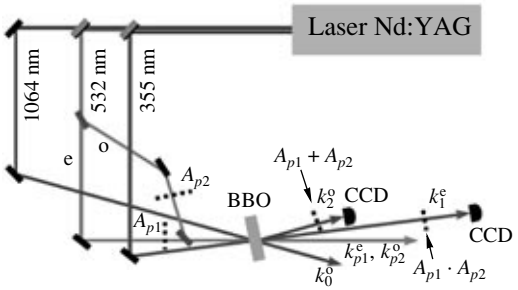

Fig. 12. Experimental setup for the implementation of the AND and OR gates. BBO, β-BaB_2O_4 crystal cut at 32°. The inputs are encoded on fields a_{p1} and a_{p2} as binary digits A_{p1} and A_{p2}, and the outputs are read on fields $a_1(z)$ and $a_2(z)$, respectively.

Figure 12 shows the setup for the realization of the AND gate. The mask on beam a_{p1} was located at a distance of $d_{O,\,kp1} = 33$ cm from the BBO, and the mask on beam a_{p2} at a distance of $d_{O,\,kp2} = 21.5$ cm. At these distances, we could neglect the diffraction effects of the holes and consider the transmitted beams as collimated [36]. The beams after the masks were superimposed at the BBO location in order to carefully match the bits of each input. Due to the geometry and the relative position of the masks, the superimposition realized all the possible permutations of the input values.

In Fig. 13c, we show the intensity modulation of the generated field $a_1(z)$ as detected with a CCD camera (interlaced, pixel dimensions 6.3 × 9.8 μm, model PE2001, Pulnix Europe, Basingstoke, United Kingdom) operated in low-resolution acquisition mode (pixel dimensions 25.2 × 39.2 μm). Note that, in all the experiments described in this work, it was not necessary to locate the detector at particular distances from the BBO, since the diffraction effects on the output beams were negligible.

We also detected with the CCD camera the images formed on the BBO entrance face of the fields transmitted by the masks. To do this, we realized a 2*f*-imaging system with a lens of focal length $f = +210$ mm. Images of the intensity distributions of fields a_{p1} and a_{p2}, recorded by averaging 50 pulses, are displayed in Figs. 13a and 13b.

The implementation of the OR gate required two seed fields, i.e., $a_0(0)$ and $a_1(0)$ (see Fig. 12), to generate field $a_2(z)$, which depends on fields a_{p1} and a_{p2} as shown in Eq. (57). The masks placed on the pump fields were the same as in the previous case and located at the same distances from the BBO. We observed the output of the OR gate along the propagation direction of field

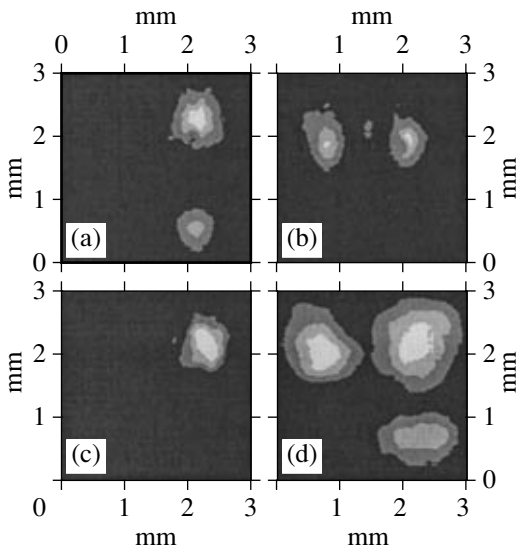

Fig. 13. Images (four gray levels) detected by the CCD camera as averages over 50 pulses relative to the AND and OR gates: (a, b) intensity maps of fields a_{p1} and a_{p2}, respectively, as detected at the BBO crystal entrance; (c) intensity map of field $a_1(z)$, which encodes the output of the AND gate; (d) intensity map of field $a_2(z)$, which encodes the output of the OR gate.

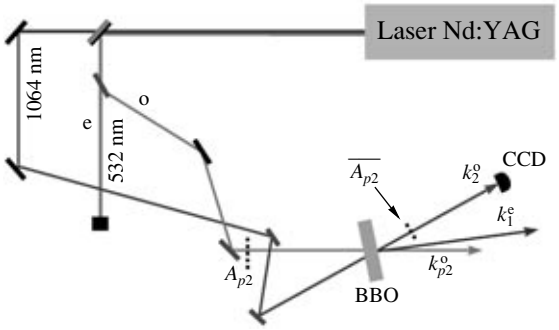

Fig. 14. Experimental setup for the implementation of the NOT gate. BBO as in Fig. 12. The binary number A_{p2} is encoded on the pump field a_{p2}; the depleted field $a_2(z)$ represents the negation of A_{p2}, while field $a_1(z)$ carries its copy.

$a_2(z)$ generated into the crystal. In Fig. 13d, we show the intensity profile of the generated field $a_2(z)$ averaged over 50 pulses as detected by the CCD camera. We must remark that, due to the particular encoding of the data, only the spot located at the upper right corner of Fig. 13d is generated by the simultaneous presence of four fields according to Eq. (57), while the other spots are generated by two fields only.

We implemented the NOT gate by the sum-frequency generation of field $a_1(z)$, with a_{p2} as the pump, $a_2(0)$ as the seed, and $a_0(0) = a_1(0) = a_{p1} = 0$ (see Eq. (54b)). As depicted in Fig. 14, the mask on field a_{p2} was located at a distance of $d_{O,kp2} = 8.5$ cm from the BBO and the seed field $a_2(0)$ propagated from the laser with a wave front flat in its central part. The flat beam is the fundamental output of the laser and remains collimated over a very long distance at the energies used in the present work. For this reason, we decided to avoid the introduction of any optical system to modify and/or improve the beam quality. The residual irregularity of the beam profile is apparent in the results. Due to the high intensity of the modulated field a_{p2}, the initially flat field $a_2(0)$ emerged depleted from the nonlinear crystal according to Eq. (59), with $|g_1|z \simeq 0.7$. The obtained depletion of field $a_2(0)$ was about 40%. In Fig. 15a, we show the 1 : 1 intensity map of field a_{p2} at the entrance face of the crystal as obtained through the $2f$-imaging system described above. In Fig. 15b, we show the intensity profile of field $a_2(z)$ recorded by the CCD: the image reveals an intensity map somehow complementary to that of input a_{p2}. Finally, Fig. 15c displays the intensity map of field $a_1(z)$, which represents the replica of the input.

Note that we only show averaged images of the AND and OR gates, since the results appear more clearly. Nevertheless, the noise was low enough to allow the correct logic values of the outputs to be read shot by shot, so that each gate can be obtained with single-shot interactions, as in the case of the NOT gate. For this reason, we can assert that our apparatus can return the outputs of the logic gates in a time as short as the pulse duration [37].

In all these experiments, we used masks that heavily shielded the input fields. However, by applying the Rayleigh criterion to the crystal entrance face, it is possible to encode as many as 10^4 bits on a mask located at 1 cm from the BBO, so that data can be encoded at high density. Moreover, diffraction caused by masks is rather irrelevant, since the two interlinked interactions produce holographic images and optical resolution can be increased.

As a further application, we have also implemented an all-optical half-adder that is able to operate in parallel on two pairs of single-digit binary numbers. In particular, we realized the sums 1 + 0 and 1 + 1 by encoding the data on four fields, that is, on the two pump fields (a_{p1} and a_{p2}) and on two seed fields ($a_0(0)$ and $a_1(0)$), and reading the result of the half-adder on the generated fields $a_2(z)$ (SUM, i.e., less significant bit) and $a_1(z)$ (CARRY, i.e., most significant bit). In addition, by duplicating the interlinked interactions in another crystal, these output fields can be frequency-converted to implement an all-optical looping circuit (see [38]).

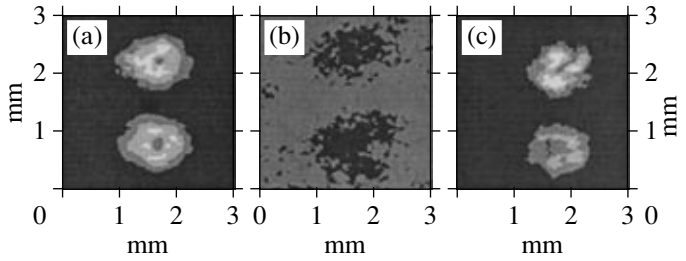

Fig. 15. Intensity maps (four gray levels) of the images detected by the CCD camera: (a) pump field a_{p2} (average over 50 shots) at the BBO crystal entrance face; (b) depleted field $a_2(z)$ (single-shot) giving the output of the NOT gate; (c) generated field $a_1(z)$ (average over 50 shots) giving the replica of the input field a_{p2}.

3.4. Three-Mode Entanglement by Parametric Interactions

We now turn to the quantum analysis of the five-mode interaction described in the previous sections and show how to realize a compact scheme to generate three-mode entanglement. As we have seen, the outmost used source of two-mode CV entanglement is the twin beams, which belong to the class of bipartite Gaussian states. In a group-algebraic language, they are the coherent states of the group $SU(1, 1)$, i.e., the states evolved from vacuum via a two-boson unitary realization of the group. Within the class of Gaussian states, the simplest generalization of twin beams to three modes is the coherent states of the group $SU(2, 1)$. Indeed, these states can be generated by multimode parametric processes with Hamiltonians that are at most bilinear in the fields. In particular, these processes involve three modes of the field, a_0, a_1, and a_2, with mode a_0 that interacts through a parametric-amplifier-like Hamiltonian with the other modes, whereas the latter interact with each other via a beam-splitter-like Hamiltonian. A particular representative of such a type of Hamiltonians is given by the following:

$$H_{\text{int}} = \gamma_0 a_0^\dagger a_2^\dagger + \gamma_1 a_1^\dagger a_2 + \text{H.c.} \tag{62}$$

The earliest studies on the dynamics and quantum properties of the states realized via Hamiltonian (62) can be traced back to the works in [39]. The relevance in studying in detail the dynamics generated by the Hamiltonian above lies in the fact that it can be realized in a variety of different contexts, from quantum optics [40–44] to condensate physics [45]. Studies have also been performed in which the coupling between two optical modes and a vibrational mode of a macroscopic object, such as a mirror, has been considered [46]. Recently, ions trapped in a cavity have also been demonstrated to realize Hamiltonian (62) for a suitable configuration [47]. In particular, the experimental realization we are more interested in involves the interlinked simultaneous interactions between three optimal modes, taking place in a single nonlinear $\chi^{(2)}$ crystal, which we discussed in detail in Section 3.1 [35]. It is immediate to see that Hamiltonian (62) admits the following constant of motion:

$$\Delta(t) \equiv N_0(t) - N_1(t) - N_2(t) \equiv \Delta(0). \tag{63}$$

In the following, we take the vacuum $|\mathbf{0}\rangle \equiv |0\rangle_0 \otimes |0\rangle_1 \otimes |0\rangle_2$ as the initial state. In this way, we describe a spontaneous three-mode process, analogous to the spontaneous downconversion leading to TWB, which cannot be described by the classical Eqs. (54). For vacuum input, we have $\Delta = 0$, i.e., $N_0(t) = N_1(t) + N_2(t)\ \forall t$. The expressions for $N_j(t)$ can be obtained by the Heisenberg evolution of the field operators which, in turn, can be calculated from the equations of motion generated by Hamiltonian (62):

$$\dot{a}_0^\dagger = i\gamma_0^* a_2, \tag{64a}$$

$$\dot{a}_1 = -i\gamma_1 a_2, \tag{64b}$$

$$\dot{a}_2 = -i\gamma_0 a_0^\dagger - i\gamma_1^* a_1. \tag{64c}$$

The above equations represent the quantum counterpart of Eqs. (51), where we made use again of the parametric approximation for the pump field and the effective coupling constants γ_0 and γ_1 have been accordingly defined. This system of differential equations can be Laplace-transformed in the following algebraic system:

$$a_0^\dagger(0) + \mu\tilde{a}_0^\dagger(\mu) = i\gamma_0^*\tilde{a}_2(\mu), \tag{65a}$$

$$a_1(0) + \mu\tilde{a}_1(\mu) = -i\gamma_1\tilde{a}_2(\mu), \tag{65b}$$

$$a_2(0) + \mu\tilde{a}_2(\mu) = -i\gamma_0\tilde{a}_0^\dagger(\mu) - i\gamma_1^*\tilde{a}_1(\mu), \tag{65c}$$

where the Laplace transform of $a_j(t)$ is given by

$$\tilde{a}_j(\mu) \equiv \int_0^\infty dt e^{-\mu t} a_j(t). \tag{66}$$

The determinant of system (65) is

$$\delta = \mu(\mu + \Gamma)(\mu - \Gamma), \tag{67}$$

where $\Gamma \equiv \sqrt{|\gamma_0|^2 - |\gamma_1|^2}$; therefore, its solution reads

$$\tilde{a}_0^\dagger(\mu) = \frac{1}{\delta}[(|\gamma_1|^2 + \mu^2)a_0^\dagger(0) + \gamma_0^*\gamma_1^* a_1(0) + i\gamma_0^*\mu a_2(0)], \quad (68a)$$

$$\tilde{a}_1(\mu) = \frac{1}{\delta}[-\gamma_0\gamma_1 a_0^\dagger(0) - i\gamma_1\mu a_2(0) + (\mu^2 - |\gamma_0|^2)a_1(0)], \quad (68b)$$

$$\tilde{a}_2(\mu) = \frac{1}{\delta}[-i\gamma_0\mu a_0^\dagger(0) - i\mu\gamma_1^* a_1(0) + \mu^2 a_2(0)]. \quad (68c)$$

The solution of system (64) follows from antitransforming Eqs. (68). We have (omitting the time dependence of the coefficients for brevity)

$$a_0^\dagger(t) = f_0 a_0^\dagger(0) + f_1 a_1(0) + f_2 a_2(0), \quad (69a)$$

$$a_1(t) = g_0 a_0^\dagger(0) + g_1 a_1(0) + g_2 a_2(0), \quad (69b)$$

$$a_2(t) = h_0 a_0^\dagger(0) + h_1 a_1(0) + h_2 a_2(0), \quad (69c)$$

where the coefficients are given by

$$f_0(t) = \frac{1}{\Omega^2}[|\gamma_0|^2\cos\Omega t - |\gamma_1|^2], \quad (70a)$$

$$f_1(t) = \frac{\gamma_0^*\gamma_1^*}{\Omega^2}[\cos\Omega t - 1], \quad (70b)$$

$$f_2(t) = i\frac{\gamma_0^*}{\Omega}\sin(\Omega t), \quad (70c)$$

$$g_0(t) = \frac{\gamma_0\gamma_1}{\Omega^2}[1 - \cos\Omega t], \quad (70d)$$

$$g_1(t) = \frac{1}{\Omega^2}[|\gamma_0|^2 - |\gamma_1|^2\cos\Omega t], \quad (70e)$$

$$g_2(t) = -i\frac{\gamma_1}{\Omega}\sin(\Omega t), \quad (70f)$$

$$h_0(t) = -i\frac{\gamma_0}{\Omega}\sin(\Omega t), \quad (70g)$$

$$h_1(t) = -i\frac{\gamma_1^*}{\Omega}\sin(\Omega t), \quad (70h)$$

$$h_2(t) = \cos(\Omega t), \quad (70i)$$

and $\Omega \equiv i\Gamma = \sqrt{|\gamma_1|^2 - |\gamma_0|^2}$. Finally, the average number of photons in each mode is

$$N_0 = N_1 + N_2, \quad (71a)$$

$$N_1 = \frac{|\gamma_0|^2|\gamma_1|^2}{\Omega^4}[\cos\Omega t - 1]^2, \quad (71b)$$

$$N_2 = \frac{|\gamma_0|^2}{\Omega^2}\sin^2(\Omega t). \quad (71c)$$

We see that, when $|\gamma_1|^2 > |\gamma_0|^2$, the dynamics is oscillatory; conversely, when $|\gamma_0|^2 > |\gamma_1|^2$, an exponential behavior is found (for a comparison between these two regimes, see [44], in which, in a quantum optical framework, the quantum dynamics of the pumps sustaining the interaction is also taken into account).

Let us now calculate explicitly the expression in the Fock representation of the state $|\Psi_2\rangle = U(t)|0, 0, 0\rangle$ evolved from vacuum via Hamiltonian (62). We can rewrite Eq. (62) as follows:

$$H_{\text{int}} = \gamma_0 K^\dagger + \gamma_1^* J + \text{h.c.}, \quad (72)$$

with the definitions $K \doteq a_0 a_2$ and $J \doteq a_1 a_2^\dagger$. To calculate the evolved state, we can proceed by factorizing the temporal evolution operator of the system; to this end, we introduce the operators $J_1 \doteq a_0 a_0^\dagger + a_2^\dagger a_2$, $J_2 \doteq a_2^\dagger a_2 - a_1^\dagger a_1$, and $M \doteq a_0 a_1$, which form with K and J a closed algebra. Actually, the temporal evolution operator can be written in the following way:

$$U(t) = e^{\beta_1 K^\dagger} e^{\beta_2 M^\dagger} e^{\beta_3 J^\dagger} e^{\beta_4 J_1} e^{\beta_5 J_2} e^{\beta_6 J} e^{\beta_7 K} e^{\beta_8 M}, \quad (73)$$

which allows us to calculate the evolution of a generic initial state as a function of β_i. Notice that the factorization above holds for a generic $SU(2, 1)$ evolution, not only for the one generated by Hamiltonian (62). By starting from vacuum, one obtains the class of coherent states of $SU(2, 1)$ group $|\Psi_2\rangle$:

$$|\Psi_2\rangle = e^{\beta_1 K^\dagger} e^{\beta_2 M^\dagger} e^{\beta_3 J^\dagger} e^{\beta_4 J_1}|0, 0, 0\rangle = e^{\beta_4} e^{\beta_1 K^\dagger}\sum_p \beta_2^p |p, p, 0\rangle = e^{\beta_4}\sum_{p, q}\beta_1^q\beta_2^p\sqrt{\frac{(p+q)!}{p!q!}}|p+q, p, q\rangle. \quad (74)$$

Notice that normalization imposes that

$$e^{\beta_4} = \sqrt{1 - |\beta_1|^2 - |\beta_2|^2}. \quad (75)$$

Since we are interested in the entanglement properties and applications of the states $|\Psi_2\rangle$, we can take the coefficients β_1 and β_2 as real numbers. In fact, one can put to zero the possible phases associated to them by performing a proper local unitary operation on mode a_1 and a_2, which, in turn, does not affect the entanglement of the state. Remarkably, the coefficients β_1 and β_2 can be easily expressed in terms of the photon number

mean value of each mode $N_k = \langle \mathbf{\Psi}_2 | a_k^\dagger a_k | \mathbf{\Psi}_2 \rangle$ ($k = 1, 2$) and N_0. By virtue of the identity

$$\sum_{n=0}^{\infty} x^n \frac{(n+a)!}{n!} = a!(1-x)^{-1-a}, \tag{76}$$

and using Eq. (75), one has

$$\begin{aligned} N_k &= e^{2\beta_4} \sum_{\{n\}} \beta_1^{2n_1} \beta_2^{2n_2} \frac{(n_1+n_2)!}{n_1! n_2!} n_k \\ &= \frac{\beta_k^2 e^{2\beta_4}}{\left(1 - \sum_k \beta_k^2\right)^2} = \beta_k^2 e^{-2\beta_4}, \end{aligned} \tag{77}$$

where $\{n\} = \{n_1, n_2\}$ and the sums over $\mathbf{n}$ are extended over natural numbers. The constant of motion (63) with $\Delta = 0$ (vacuum input) now allows one to re-express the normalization coefficient as $e^{\beta_4} = (1 + N_0)^{-1/2}$, from which, in turn, it follows that $\beta_k = \sqrt{N_k/(1+N_0)}$.

The Wigner function associated with the coherent state of $SU(2, 1)$ can now be obtained by recalling that, being evolved with a bilinear Hamiltonian from the vacuum, the states $|\mathbf{\Psi}_2\rangle$ are pure Gaussian states. As a consequence, they are completely characterized by their covariance matrix $\boldsymbol{\sigma}_2$. In order to calculate $\boldsymbol{\sigma}_2$, let us explicitly evaluate the following expectation value over the state $|\mathbf{\Psi}_2\rangle$:

$$\begin{aligned} \langle a_0 a_k \rangle &= e^{2\beta_4} \beta_k \sum_{\{n\}} \beta_1^{2n_1} \beta_2^{2n_2} \frac{(n_1+n_2)!}{n_1! n_2!} (n_1 + n_2 + 1) \\ &= \beta_k (N_1 + N_2 + 1) = \sqrt{N_k (1+N_0)}, \end{aligned} \tag{78}$$

where we repeatedly used the identity (76). Analogously, one finds that $\langle a_0^\dagger a_k \rangle = 0$, whereas $\langle a_1 a_2^\dagger \rangle = \langle a_2 a_1^\dagger \rangle = \sqrt{N_1 N_2}$ and $\langle a_1 a_2 \rangle = 0$. As a consequence, recalling the Cartesian decomposition of position and momentum operators, the expression for the covariance matrix of a $SU(2, 1)$ coherent state follows by substitution

$$\boldsymbol{\sigma}_2 = \begin{pmatrix} \mathcal{N}_0 & \mathcal{A}_1 & \mathcal{A}_2 \\ \mathcal{A}_1 & \mathcal{N}_1 & \mathcal{B}_{1,2} \\ \mathcal{A}_2 & \mathcal{B}_{1,2} & \mathcal{N}_2 \end{pmatrix}, \tag{79}$$

where the entries are given by the following 2×2 matrices ($h = 0, \ldots, 2$, $k = 1, 2$):

$$\mathcal{N}_h = \left(N_h + \frac{1}{2}\right) 1, \tag{80}$$

$$\mathcal{A}_k = \sqrt{N_k (N_0 + 1)}\, \mathbb{P}, \tag{81}$$

$$\mathcal{B}_{1,2} = \sqrt{N_1 N_2}\, 1, \tag{82}$$

with $1 = \mathrm{Diag}(1, 1)$ and $\mathbb{P} = \mathrm{Diag}(1, -1)$.

The main feature of the states $|\mathbf{\Psi}_2\rangle$ is that they are fully inseparable, i.e., inseparable with respect with any grouping of the modes. This can be explicitly demonstrated by considering the positive partial transpose criterion for each possible grouping of the modes, whose application is in turn straightforward in terms of the covariance matrix $\boldsymbol{\sigma}_2$ given in Eq. (79). Furthermore, the state $|\mathbf{\Psi}_2\rangle$ allows for high violations of tripartite Bell inequalities, as pointed out in [48, 49].

The explicit calculation above now allows one to calculate the state $|\mathbf{\Psi}_{2,\alpha}\rangle$ generated by Hamiltonian (62) starting from a coherent state of amplitude α in one of the modes, rather than from the vacuum. This may be of interest from the experimental point of view, since seeding a crystal with a coherent beam is a useful technique to align the setup and allows the verification of the classical evolution of the interacting fields, as we have seen in Section 3.1. Seeding mode a_0 and recalling Eq. (73), we have

$$\begin{aligned} |\mathbf{\Psi}_{2,\alpha}\rangle &= U(t) D_0(\alpha) |0, 0, 0\rangle \\ &= U(t) e^{-\frac{|\alpha|^2}{2}} \sum_n \frac{\alpha^n}{\sqrt{n!}} |n, 0, 0\rangle \\ &= e^{-\frac{|\alpha|^2}{2}} e^{\beta_1 K^\dagger} e^{\beta_2 M^\dagger} e^{\beta_3 J^\dagger} e^{\beta_4 J_1} \sum_n \frac{\alpha^n}{\sqrt{n!}} |n, 0, 0\rangle \\ &= e^{-\frac{|\alpha|^2}{2}} e^{\beta_1 K^\dagger} e^{\beta_2 M^\dagger} e^{\beta_3 J^\dagger} e^{\beta_4} \sum_n \frac{(\alpha e^{\beta_4})^n}{\sqrt{n!}} |n, 0, 0\rangle \\ &= e^{-\frac{|\alpha|^2}{2}} e^{\beta_4} e^{\beta_1 K^\dagger} \sum_{n,p} \frac{(\alpha e^{\beta_4})^n}{\sqrt{n!}} \frac{\beta_2^p}{\sqrt{p!}} \frac{\sqrt{(n+p)!}}{\sqrt{n!}} |n+p, p, 0\rangle \\ &= e^{-\frac{|\alpha|^2}{2}} e^{\beta_4} \sum_{n,p,q} \beta_1^q \beta_2^p (\alpha e^{\beta_4})^n \\ &\quad \times \frac{\sqrt{(n+p+q)!}}{n! \sqrt{p! q!}} |n+p+q, p, q\rangle. \end{aligned} \tag{83}$$

Furthermore, the populations with initial vacuum $N_j = \langle \mathbf{\Psi}_2 | a_j^\dagger a_j | \mathbf{\Psi}_2 \rangle$ and initial seed $N_{j\alpha} = \langle \mathbf{\Psi}_{2,\alpha} | a_j^\dagger a_j | \mathbf{\Psi}_{2,\alpha} \rangle$ are related as follows ($k = 1, 2$):

$$N_0 = \frac{N_{0\alpha} - |\alpha|^2}{1 + |\alpha|^2}, \quad N_k = \frac{N_{k\alpha}}{1 + |\alpha|^2}. \tag{84}$$

As we have already noticed, the state $|\mathbf{\Psi}_2\rangle$ is fully inseparable. The same property also holds for the state $|\mathbf{\Psi}_{2,\alpha}\rangle$, since the latter is endowed with the same cova-

riance matrix of $|\Psi_2\rangle$ [59], i.e., Eq. (79). However, notice that the state $|\Psi_{2,\alpha}\rangle$ no longer belongs to the class of coherent states of $SU(2, 1)$ (Eq. (63) is no longer satisfied starting from vacuum). This is due to the fact that the generators themselves of the harmonic oscillator algebra (to which the displacement operator $D_0(\alpha)$ belongs) do not belong to the algebra of $SU(2, 1)$, as we can see from Eq. (73).

Another interesting class of tripartite states for CV systems has been proposed by van Loock and Braunstein [50], and its experimental realization has been reported in [51]. This type of state is a very natural and scalable way to produce multimode entanglement using only passive optical elements and single squeezers. They are generated with the aid of three single-mode squeezed states combined in a "tritter" (a three-mode generalization of a beam splitter). The evolution is then ruled by a cascade of single- and two-mode quadratic Hamiltonians, not belonging, however, to the $SU(2, 1)$ group. Being generated from vacuum, the three-mode entangled states, which we denote with ϱ_t, are Gaussian with covariance matrix

$$\boldsymbol{\sigma}_t = \begin{pmatrix} \mathcal{R} & 0 & \mathcal{S} & 0 & \mathcal{S} & 0 \\ 0 & \mathcal{T} & 0 & -\mathcal{S} & 0 & -\mathcal{S} \\ \mathcal{S} & 0 & \mathcal{R} & 0 & \mathcal{S} & 0 \\ 0 & -\mathcal{S} & 0 & \mathcal{T} & 0 & -\mathcal{S} \\ \mathcal{S} & 0 & \mathcal{S} & 0 & \mathcal{R} & 0 \\ 0 & -\mathcal{S} & 0 & -\mathcal{S} & 0 & \mathcal{T} \end{pmatrix}, \tag{85}$$

where $\mathcal{R} = \frac{1}{2}\left(\cosh 2r + \frac{1}{3}\sinh 2r\right)$, $\mathcal{T} = \frac{1}{2}\left(\cosh 2r - (1/3)\sinh 2r\right)$, $\mathcal{S} = -\frac{2}{3}\cosh r \sinh r$, and r is a generalized squeezing parameter. Notice that, by calculating the average photon numbers from the covariance matrix $\boldsymbol{\sigma}_t$, it immediately follows that the state ϱ_t does not belong to the class of the coherent states of $SU(2, 1)$, since Eq. (63) is not satisfied.

The covariance matrix (85) is symmetric under permutation of the modes. With a slightly different generation strategy, one can recover the covariance matrix (79) (asymmetric under permutation), still within a cascading interaction scheme [52]. Consider in fact a two-mode squeezing interaction between modes a_0 and a_2 (which, in turn, can be produced by mixing two squeezed vacua in a balanced beam splitter):

$$S_2(\lambda_0) = \exp\{\lambda_0 a_0^\dagger a_2^\dagger - \lambda_0^* a_0 a_2\}, \tag{86}$$

followed by a two-mode mixing interaction between modes a_1 and a_2:

$$U(\lambda_1) = \exp\{\lambda_1 a_1^\dagger a_2 - \lambda_1^* a_1 a_2^\dagger\}. \tag{87}$$

Physically, this simply means inserting a beam splitter on one mode of a twin beam. By defining $\lambda_0 = re^{i\varphi}$, $\mu = \cosh r$, $\nu = e^{i\varphi}\sinh r$, and $\lambda_1 = \phi e^{i\theta}$, the evolved state in the Fock representation reads as follows:

$$\begin{aligned} &U(\lambda_1)S_2(\lambda_0)|0, 0, 0\rangle \\ &= \exp\{e^{i\theta}\tan\phi a_1^\dagger a_2\}(\cos\phi)^{a_2^\dagger a_2 - a_1^\dagger a_1} \\ &\times \exp\{-e^{-i\theta}\tan\phi a_1 a_2^\dagger\}\frac{1}{\mu}\sum_{k=0}^{\infty}\left(\frac{\nu}{\mu}\right)^k |k, 0, k\rangle, \end{aligned} \tag{88}$$

where we have disentangled the two-mode mixing operator. It is now straightforward to obtain the following expression:

$$\begin{aligned} &U(\lambda_1)S_2(\lambda_0)|0, 0, 0\rangle \\ &= \frac{1}{\mu}\sum_{p, q=0}^{\infty}\left(\frac{\nu}{\mu}\cos\phi\right)^p\left(\frac{\nu}{\mu}e^{i\theta}\sin\phi\right)^q\sqrt{\frac{(p+q)!}{q!p!}}|p+q, q, p\rangle. \end{aligned} \tag{89}$$

For real coupling constants (e.g., $\theta = \varphi = 0$), one regains the expression in Eq. (74), with $N_0 = \nu^2$, $N_1 = \nu^2\sin^2\phi$, and $N_2 = \nu^2\cos^2\phi$. As a consequence, the covariance matrix (79) is recovered.

3.5. Applications: Symmetric and Asymmetric Telecloning

Let us now consider an application of the tripartite entangled state $|\Psi_2\rangle$ introduced above to quantum information processing. Suppose that one wants to remotely clone an unknown quantum state to two distant receivers, and he is not able to directly transfer either the original state or the two copies (for the case in which direct transmission is a possible option, see [53]). Quantum mechanics allows this goal to be achieved in two steps. One may first locally produce two copies of the original state by means of a cloning protocol. Then, the teleportation of each copy allows one to attain the transfer of information. This strategy has the obvious advantage of using only bipartite entangled sources. Of course, an analogous strategy in which the original state is first teleported and then cloned can be taken into account. However, in any of the two cases and even in the absence of losses, the receivers are not left with two optimum clones of the original state, due to the nonunitary fidelity of the teleportation protocol in the case of finite energy. This obstacle may be circumvented by pursuing a one-step strategy consisting of a *nonlocal* cloning. By this, we mean that the cloning process is supported by a tripartite entangled state, which is distributed among all the parties involved. This so-called *telecloning* process is thus nonlocal in the sense that it proceeds along the lines of a natural generalization of the teleportation protocol to the many-recipient case [54]. Recall that CV teleportation is based on the twin beams, i.e., the coherent states of the group $SU(1, 1)$, which provide the shared entangle-

ment needed to support the protocol. Thus, in order to implement a multipartite version of the teleportation protocol, one is naturally led to consider as shared entangled states the ones introduced above, i.e., the coherent states of the group $SU(2, 1)$. In the following, we will analyze in detail the case of $1 \longrightarrow 2$ telecloning, both when the tripartite state used to support the telecloning protocol is generated from vacuum and from a coherent seed. Both symmetric and asymmetric cloning will be considered, and the question of the optimality of the protocol will be addressed.

A schematic diagram of the telecloning process is depicted in Fig. 16. After the preparation of the state $|\mathbf{\Psi}_2\rangle$, a joint measurement is made on the mode a_0 and the mode b to be telecloned, which corresponds to the measurement of the complex amplitude $Z = b + a_0^\dagger$, as in the case of the teleportation protocol. The whole measurement is described by the POVM $\Pi(z)$ acting on the mode a_0, namely, $\Pi(z) = \pi^{-1}D(z)\varrho_{\text{in}}^T D^\dagger(z)$, where ϱ_{in} is the state to be teleported and cloned. The probability distribution of the outcomes is given by

$$\begin{aligned} P(z) &= \mathrm{Tr}_{012}[|\mathbf{\Psi}_2\rangle\langle\mathbf{\Psi}_2|\Pi(z)\otimes\mathbb{I}_1\otimes\mathbb{I}_2] \\ &= \frac{1}{\pi(1+N_0)}\sum_{pq}\frac{N_1^p N_2^q}{(1+N_0)^{p+q}}\frac{(p+q)!}{p!q!} \\ &\quad\times\langle p+q|D(z)\varrho_{\text{in}}^T D^\dagger(z)|p+q\rangle. \end{aligned} \tag{90}$$

The conditional state of the mode a_1 and a_2 after the outcome z is given by

$$\begin{aligned} \varrho_z &= \frac{1}{P(z)}\mathrm{Tr}_0[|\mathbf{\Psi}_2\rangle\langle\mathbf{\Psi}_2|\Pi(z)\otimes\mathbb{I}_1\otimes\mathbb{I}_2] \\ &= \frac{1}{P(z)}\frac{1}{\pi(1+N_0)}\sum_{p,q}\sum_{k,l}\sqrt{\frac{N_1^{p+k}N_2^{q+l}}{(1+N_0)^{p+q+k+l}}} \\ &\quad\times\sqrt{\frac{(p+q)!}{p!q!}\frac{(k+l)!}{k!l!}}\langle k+l|D(z)\varrho_{\text{in}}^T D^\dagger(z)|p+q\rangle\langle k,l|. \end{aligned} \tag{91}$$

After the measurement, the conditional state should be transformed by a further unitary operation, depending on the outcome of the measurement. In our case, this is a two-mode product displacement

$$U_z = D_1^T(z)\otimes D_2^T(z). \tag{92}$$

This is a local transformation, which generalizes to two modes the procedure already used in the original continuous variable teleportation protocol. The overall state of the two modes is obtained by averaging over the possible outcomes:

$$\varrho_{12} = \int_{\mathbb{C}} d^2 z P(z)\tau_z, \tag{93}$$

where $\tau_z = U_z\varrho_z U_z^\dagger$.

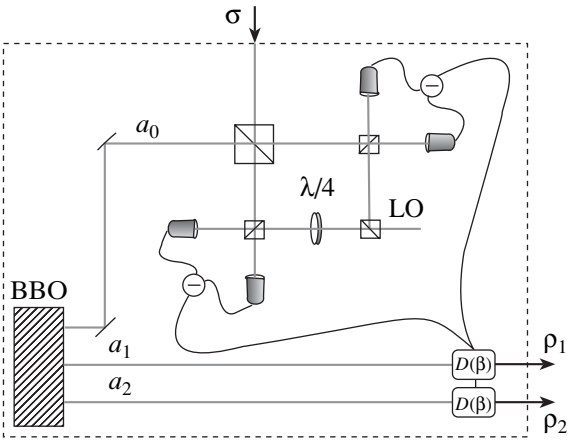

Fig. 16. Schematic diagram of the $1 \longrightarrow 2$ telecloning scheme described in the text.

If b is excited in a coherent state $\sigma = |\alpha\rangle\langle\alpha|$, then the probability of the outcomes is given by

$$P_\alpha(z) = \frac{1}{\pi(1+N_0)}\exp\left\{-\frac{|z+\alpha^*|^2}{1+N_0}\right\}. \tag{94}$$

Moreover, since the POVM is pure, the conditional state is also pure. In this way, we find that $\varrho_z = |\psi_z\rangle\rangle\langle\langle\psi_z|$ is the product of two states, namely,

$$|\psi_z\rangle\rangle = |(\alpha+z^*)\beta_1\rangle\otimes|(\alpha+z^*)\beta_2\rangle, \tag{95}$$

where we recall that $\beta_h = \sqrt{N_h/(1+N_0)}$, with $h = 1, 2$. Correspondingly, we have $\tau_z = U_z|\psi_z\rangle\rangle\langle\langle\psi_z|U_z^\dagger$ with

$$\begin{aligned} &U_z|\psi_z\rangle\rangle \\ &= |\alpha\beta_1 + z^*(\beta_1-1)\rangle\otimes|\alpha\beta_2+z^*(\beta_2-1)\rangle. \end{aligned} \tag{96}$$

The partial traces $\varrho_1 = \mathrm{Tr}_2[\varrho_{12}]$ and $\varrho_2 = \mathrm{Tr}_1[\varrho_{12}]$ read as follows:

$$\begin{aligned} \varrho_h &= \int_{\mathbb{C}} d^2 z P_\alpha(z) \\ &\quad\times|\alpha\beta_h + z^*(\beta_h-1)\rangle\langle\alpha\beta_h+z^*(\beta_h-1)|. \end{aligned} \tag{97}$$

Upon changing the integration variable, we obtain the following expression for the clones:

$$\varrho_h = \int_{\mathbb{C}} d^2 w\frac{1}{\pi n_h}\exp\left\{-\frac{|w-\alpha|^2}{n_h}\right\}|w\rangle\langle w|, \tag{98}$$

where we have defined

$$n_h = (\sqrt{N_0+1}-\sqrt{N_h})^2. \tag{99}$$

From expression (98), one immediately recognizes that the clones are given by thermal states $\varrho_{\text{th}}(n_h)$ with mean

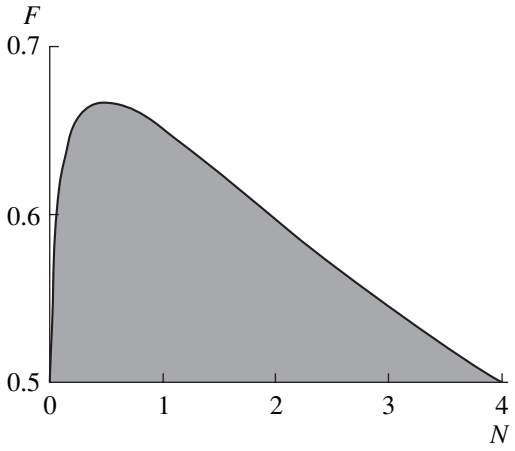

Fig. 17. Fidelity of symmetric clones versus the average (equal) photon number N of modes a_1 and a_2.

photon number n_h, displaced by the amount α, namely,

$$\varrho_h = D_h(\alpha)\varrho_{\rm th}(n_h)D_h^\dagger(\alpha). \qquad (100)$$

As a consequence, we see that the protocol acts like a proper covariant Gaussian cloning machine [55] and that the noise introduced by the cloning process is entirely quantified by the thermal photons n_h, which, in turn, depend only on the value of the mean photon numbers N_h of the shared state. Furthermore, this implies that the two clones can either be equal to one each other or different. In other words, a remarkable feature of this scheme is that it is suitable to realize both symmetric cloning, when $N_1 = N_2 = N$, and asymmetric cloning, $N_1 \neq N_2$. This arises as a consequence of the possible asymmetry of the state that supports the teleportation.

Let us first consider the case of symmetric cloning. For a given generation process of the state $|\Psi_2\rangle$, we pointed out that the symmetric condition $N_1 = N_2 = N$ has to be satisfied in order to produce two equal clones. For example, if one considers the interaction in Eq. (62), this condition is achieved when the coupling constants γ_0 and γ_1 are set such that

$$\cos(\Omega t) = \frac{|\gamma_0|^2}{2|\gamma_1|^2 - |\gamma_0|^2}, \qquad (101a)$$

$$N = \frac{4|\gamma_0|^2|\gamma_1|^2}{(2|\gamma_1|^2 - |\gamma_0|^2)^2}, \qquad (101b)$$

according to Eqs. (71). The fidelity of the clones is given by (we put $n_1 = n_2 = n$)

$$F = \frac{1}{1+n} = (2 + 3N - 2\sqrt{N(2N+1)})^{-1}. \qquad (102)$$

As we expect from a proper cloning machine, the fidelity is independent of the amplitude of the initial signal, and, for $0 < N < 4$, it is larger than the classical limit $F = 1/2$. In Fig. 17, the behavior of the fidelity versus the average photon number N is shown in the relevant regime. We can see that the fidelity reaches its maximum $F = 2/3$ for $N = 1/2$. For example, when $|\Psi_2\rangle$ is produced via Hamiltonian (62), this means that optimal cloning is achieved when the coupling constants are chosen such that $|\gamma_0/\gamma_1| = (6 - \sqrt{32})^{1/2} \simeq 0.586$, according to Eqs. (101). The total mean photon number required to reach optimal telecloning is thus $N_0 + N_1 + N_2 = 2$; hence, as we stated above, it can be achieved without the need of infinite energy. This is an extremely interesting feature of the telecloning protocol, which, as already noticed, cannot be achieved via local cloning and teleportation. The scheme presented is the analogue of that in [52]. There, the telecloning is supported by a state $|\Psi_2\rangle$ produced by means of a cascading process, as described above [see, in particular, Eq. (89)]. Of course, both the protocols described here and in [52] achieve optimality by relying on minimal energetic resources; i.e., the total mean photon number is 2 in both cases.

Let us now consider the asymmetric case. For $N_1 \neq N_2$, the fidelities of the two clones are given by $F_h = (1 + n_h)^{-1}$, i.e.,

$$F_h = (2 + N_h + 2N_k - 2\sqrt{N_h(N_0+1)})^{-1}, \qquad (103)$$

where $h, k = 1, 2$ $(h \neq k)$. A question arises as to whether it is possible to set the values of N_1 and N_2 in order to obtain a fidelity larger than the bound $F = 2/3$ for one of the clones, say ϱ_1, while accepting a decreased fidelity for the other clone. For instance, if the state $|\Psi_2\rangle$ is generated via interaction (62), one can vary the mean photon number in each mode by tuning the coupling constants γ_0 and γ_1 [see Eqs. (71)], which, in turn, can be done by acting on the pump intensities. In particular, if we impose $F_2 = 1/2$, i.e., the minimum value to assure the genuine quantum nature of the telecloning protocol, we can maximize F_1 by properly choosing the states $|\Psi_2\rangle$. The maximum value turns out to be $F_{2,\max} = 4/5$, and it corresponds to the choice $N_2 = 1/4$ and $N_1 = 1$. More generally, one can fix F_2; then, the maximum value of F_1 is obtained choosing $N_1 = (1/F_2 - 1)$ and $N_2 = (4/F_2 - 4)^{-1}$. The relation between the fidelities is then

$$F_1 = 4\frac{(1-F_2)}{(4-3F_2)}, \qquad (104)$$

which shows that F_1 is a decreasing function of F_2 and that $2/3 < F_1 < 4/5$ when $1/2 < F_2 < 2/3$ (see light gray area in Fig. 18).

The comparison with the general bound for $1 \longrightarrow 2$ cloning of coherent states given in [56] allows us to conclude that the protocol described realizes an optimal asymmetric cloning of coherent states. The sum of the two fidelities $F_1 + F_2 = 1 + 3F_1F_2/4$ is maximized in the

symmetric case in which the optimal fidelity $F_1 = F_2 = 2/3$ can be reached. The role of ϱ_1 and ϱ_2 can be exchanged, and the above considerations still hold.

We now show that the protocol above can also be implemented when the state that supports teleportation does not belong to the class of coherent states of $SU(2, 1)$. In particular, we focus our attention on the case in which the support's state is generated by Hamiltonian (62) starting from a coherent state in one of the modes, rather than from the vacuum, i.e., the state $|\mathbf{\Psi}_{2,\alpha}\rangle$ in Eq. (83). As we saw in Section 3.1, this is relevant from an experimental point of view.

The analysis of the scheme follows the lines of the protocol described above. Recalling Eqs. (83) and (84), the state $|\mathbf{\Psi}_{2,\alpha}\rangle$ is given by

$$|\mathbf{\Psi}_{2,\alpha}\rangle = e^{-\frac{|\alpha|^2}{2}}\left(\frac{1+|\alpha|^2}{1+N_{0\alpha}}\right)^{\frac{1}{2}}\sum_{npq}\alpha^n\left(\frac{1+|\alpha|^2}{1+N_{0\alpha}}\right)^{n/2} \times\left(\frac{N_{1\alpha}}{1+N_{0\alpha}}\right)^{p/2}\left(\frac{N_{2\alpha}}{1+N_{0\alpha}}\right)^{q/2} \times\frac{1}{n!}\sqrt{\frac{(n+p+q)!}{p!q!}}|n+p+q, p, q\rangle, \quad (105)$$

whereas conservation law (63) implies that

$$N_{0\alpha} - N_{1\alpha} - N_{2\alpha} = |\alpha|^2. \quad (106)$$

A more useful expression for state (105) is the following:

$$|\mathbf{\Psi}_{2,\alpha}\rangle = D_0(\alpha f_0(-t)) \otimes D_1(-\alpha^* f_1^*(-t)) \otimes D_2(-\alpha^* f_2^*(-t))|\mathbf{\Psi}_2\rangle, \quad (107)$$

where $f_j(t)$, $j = 0, 1, 2$, are given in Eqs. (70). Expression (107) can be easily derived by using the Heisenberg equation of motion for the field mode $a_0(t)$ (see Eqs. (69)). The joint measurement described by the POVM $\Pi(\beta)$ now gives the following probability distribution:

$$P(\beta) = \mathrm{Tr}_{012}[|\mathbf{\Psi}_{2,\alpha}\rangle\langle\mathbf{\Psi}_{2,\alpha}|\Pi(\beta)\otimes\mathbb{I}_1\otimes\mathbb{I}_2] = \frac{1}{\pi(1+N_0)}\sum_{pq}\frac{N_1^p N_2^q}{(1+N_0)^{p+q}}\frac{(p+q)!}{p!q!} \times{}_0\langle\psi_{p+q}|D(\beta)\sigma^T D^\dagger(\beta)|\psi_{p+q}\rangle_0, \quad (108)$$

where we have calculated the trace over the shifted Fock basis defined by $|\psi_n\rangle_0 \equiv D_0(\alpha f_0)|n\rangle_0$, and $|\psi_n\rangle_j \equiv D_j(-\alpha^* f_j^*)|n\rangle_j$, $j = 1, 2$. Notice that, in Eq. (108), $N_j = \langle\mathbf{\Psi}_2|a_j^\dagger a_j|\mathbf{\Psi}_2\rangle$ are the average photon numbers for the initial vacuum state, i.e., the quantities given in Eqs. (71). Recall that the latter are connected with the populations for seeded crystal $N_{j\alpha} = \langle\mathbf{\Psi}_{2,\alpha}|a_j^\dagger a_j|\mathbf{\Psi}_{2,\alpha}\rangle$ through Eqs. (84). The conditional state of the modes a_1 and a_2 after the outcome β is now

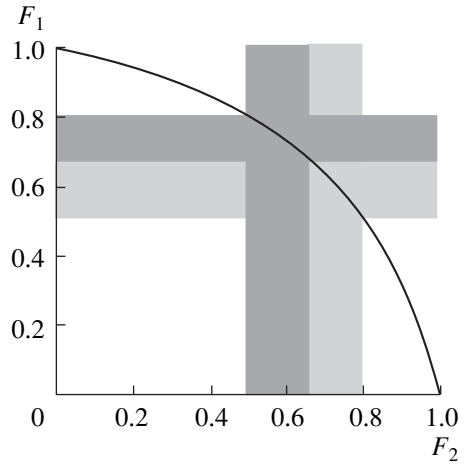

Fig. 18. Relation between the fidelities of the two clones in the asymmetric telecloning protocol (see text for details).

$$\varrho_\beta = \frac{1}{P(\beta)}\mathrm{Tr}_1[|\mathbf{\Psi}_{2,\alpha}\rangle\langle\mathbf{\Psi}_{2,\alpha}|\Pi(\beta)\otimes\mathbb{I}_1\otimes\mathbb{I}_2] = \frac{1}{P(\beta)}\frac{1}{\pi(1+N_0)}\sum_{pqkl}\frac{N_1^{(p+k)/2}N_2^{(q+l)/2}}{(1+N_0)^{(p+q+k+l)/2}} \times\sqrt{\frac{(p+q)!(k+l)!}{p!q!k!l!}}\langle\psi_{k+l}|D(\beta)\sigma^T D^\dagger(\beta)|\psi_{p+q}\rangle \times|\psi_p, \psi_q\rangle\langle\psi_k, \psi_l|. \quad (109)$$

If the reference mode b is excited in a coherent state $\boldsymbol{\sigma} = |z\rangle\langle z|$, then the distribution of the outcomes is given by

$$P_z(\beta) = \frac{1}{\pi(1+N_0)}\exp\left\{-\frac{|\beta + z^* - \alpha f_0|^2}{1+N_0}\right\}. \quad (110)$$

As above, the conditional state is pure: $\varrho_\beta = |\psi_\beta\rangle\rangle\langle\langle\psi_\beta|$, with

$$|\psi_\beta\rangle\rangle = |\zeta_{1\beta}\rangle_1 \otimes |\zeta_{2\beta}\rangle_2, \quad (111)$$

i.e., the product of two independent coherent states. The amplitudes are given by

$$\zeta_{1\beta} = (z + \beta^* - \alpha^* f_0^*)\beta_1 - \alpha^* f_1^*, \quad \zeta_{2\beta} = (z + \beta^* - \alpha^* f_0^*)\beta_2 - \alpha^* f_2^*, \quad (112)$$

where the quantities β_h (with $h = 1, 2$) are again given by $\beta_h = \sqrt{N_h/(1+N_0)}$. We now need a unitary transformation acting differently on the modes a_1 and a_2, with respect to the previous section. The following displace-

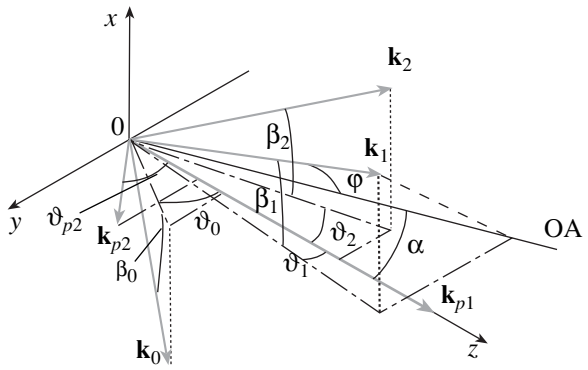

Fig. 19. Scheme of the interaction inside the crystal: ϑ_j, angles in the plane (y, z); β_j, angles of each wave vector with respect to this plane; α, tuning angle; $\mathbf{k}_j^{o,e}$, wave vectors of the interacting fields.

ment transformation does not depend on the initial amplitude z and allows cloning at a distance:

$$U_\beta = D_1^\dagger(\beta^* - \beta_1\alpha^* f_0^* - \alpha^* f_1^*) \otimes D_2^\dagger(\beta^* - \beta_2\alpha^* f_0^* - \alpha^* f_2^*). \quad (113)$$

Indeed, the output conditional state coincides with that of Eq. (96), such that the partial traces are identical to those given in Eq. (100). For $N_1 = N_2 = N$, we obtain symmetric clones with the same fidelity as in Eq. (102). Furthermore, conditions (101) still hold. Notice also that the protocol for asymmetric cloning can be straightforwardly extended to the present seeded scheme. In addition, it is possible to extend the protocol above to the case of $1 \longrightarrow m$ telecloning of generic Gaussian pure states, both for the case of symmetric and completely asymmetric cloning [57]. The effect of noise on the protocol has also been studied, showing that optimality can still be attained even in the presence of losses in the propagation line between the sender and the receivers, for propagation times diverging as the number of modes m increases [57].

We finally mention that other possible applications of the tripartite entangled state $|\Psi_2\rangle$ have been studied. The conditional state generation of two-mode states, both Gaussian and non-Gaussian, has been analyzed in [40, 49]. In the latter case, an enhancement of nonlocal correlation has been pointed out with respect to a standard twin beam. The application of the telecloning protocol described above to quantum information distribution in an amplitude-modulated communication scenario has also been pointed out in [53], showing the advantages of such a scheme with respect to a local strategy.

3.6. The Three-Mode State Generation

In Section 2.3, we described the production of the SPDC obtained by sending an intense pump beam into a BBO crystal. In particular, we showed the dependence of the characteristic cones on some parameters, such as the tuning angle α and the signal wavelength.

The generation of a three-mode state is more complex to explain due to the presence of two pump fields instead of only one [58].

To better understand this process, it is convenient to assume that the wave vector $\mathbf{k}_{p1}$ relative to the pump field a_{p1} is normal to the crystal entrance face and propagates along the z axis of the medium. With reference to Fig. 19, we assume that the wave vector $\mathbf{k}_{p2}$ corresponding to the other pump field a_{p2} lies in the plane (y, z) formed by the optical axis (OA) of the crystal and the wave vector $\mathbf{k}_{p1}$. We indicate as ϑ_j the angles in the plane (y, z) formed by each wave vector with $\mathbf{k}_{p1}$ and as β_j the angles of each wave vector with respect to this plane. Under these hypotheses, we have $\beta_{p1} = \vartheta_{p1} = 0$ and $\beta_{p2} = 0$. In order to calculate a set of internal angles suitable for the realization of the process, it is convenient to write the projection of the phase-matching conditions along the three Cartesian axes (x, y, z). We thus obtain two systems, each formed by three equations, i.e.,

$$k_0\sin\beta_0 + k_2\sin\beta_2 = 0, \quad (114a)$$

$$k_0\cos\beta_0\sin\vartheta_0 + k_2\cos\beta_2\sin\vartheta_2 = 0, \quad (114b)$$

$$k_0\cos\beta_0\cos\vartheta_0 + k_2\cos\beta_2\cos\vartheta_2 = k_{p1} \quad (114c)$$

for the SPDC and

$$k_1\sin\beta_1 = k_2\sin\beta_2, \quad (115a)$$

$$k_1\cos\beta_1\sin\vartheta_1 = k_2\cos\beta_2\sin\vartheta_2 + k_{p2}\sin\vartheta_{p2}, \quad (115b)$$

$$k_1\cos\beta_1\cos\vartheta_1 = k_2\cos\beta_2\cos\vartheta_2 + k_{p2}\cos\vartheta_{p2} \quad (115c)$$

for the other interaction. In addition, we have the following definitions:

$$k_1(\alpha, \vartheta_1, \beta_1) = \frac{\omega_1}{c}n_1(\alpha, \vartheta_1, \beta_1) = \frac{\omega_1}{c}\left(\frac{\cos^2(\alpha - \vartheta_1)\cos^2(\beta_1)}{n_o^2(\omega_1)} + \frac{1 - \cos^2(\alpha - \vartheta_1)\cos^2(\beta_1)}{n_e^2(\omega_1)}\right)^{-1/2}, \quad (116a)$$

$$k_{p1}(\alpha) = \frac{\omega_{p1}}{c}n_{p1}(\alpha) = \frac{\omega_{p1}}{c}\left(\frac{\cos^2\alpha}{n_o^2(\omega_{p1})} + \frac{\sin^2\alpha}{n_e^2(\omega_{p1})}\right)^{-1/2}. \quad (116b)$$

As we have eight variables and only six equations, we can solve the two systems by taking ϑ_{p2} and α as parameters [58]. In particular, we can study the solu-

tions for the angles ϑ_j and β_j as functions of ϑ_{p2} and for a given value of the tuning angle α. For some angles, two solutions exist instead of one: for example, we obtain two values for each β_j, so that we have a symmetry with respect to the (y, z) plane just as in the TWB generation. Moreover, we have two solutions for ϑ_0 and ϑ_2: this means that we also have a symmetry with respect to the z axis. Obviously, as for the SPDC generation, these solutions are coupled in order to fulfill Eqs. (114). For each pair of ϑ_0 and ϑ_2, there are two possible choices of ϑ_{p2}, but once we have fixed it only one solution for ϑ_1 exists. For the sake of clarity, let us first discuss the solutions in the plane (y, z): in particular, for $\lambda_0 = 778.2$ nm, $\lambda_1 = 394.4$ nm, $\lambda_2 = 632.8$ nm, $\lambda_{p1} = 349$ nm, and $\lambda_{p2} = 1047$ nm, four sets of angles ϑ_j exist that simultaneously satisfy systems (114) and (115). To realize the interactions, we chose the following configuration: $\vartheta_0 = -1.35°$, $\vartheta_1 = -6.45°$, $\vartheta_2 = 1.09°$, $\vartheta_{p2} = -19.10°$, with $\alpha = 33.75°$ and $\vartheta_{CUT} = 38.4°$. By applying Snell's law to the set, for a crystal with $\vartheta_{CUT} = 38.4°$, we obtain the external angles, i.e., $\vartheta_{0ext} = -2.26°$, $\vartheta_{1ext} = -10.71°$, $\vartheta_{2ext} = 1.85°$, $\vartheta_{p2ext} = -32.15°$, calculated with respect to the propagation direction of pump a_4 outside the crystal.

In order to study the process in space, it is worthwhile to analyze the dependence of all the angles (β_j and ϑ_j) on the parameters α, ϑ_{p2}, and also on λ_0. For example, Fig. 20 displays the solution for the internal angles ϑ_0, ϑ_1, ϑ_2, and ϑ_{p2} as functions of α for $\lambda_0 = 778.2$ nm, while Fig. 21a is a plot of the generated field a_1 on a plane beyond the BBO and orthogonal to the propagation direction of the pump a_{p1}.

Notice that, for fixed values of the tuning angle and of the angle ϑ_{p2}, this field, which consists of two polychromatic half-moons, is symmetric with respect to the plane (y, z) and that only one solution exists in the plane itself, represented by a spot, having the wavelength $\lambda_1 = 394.4$ nm. Figure 21b is a picture of the half-moons taken on a screen located outside the crystal. Note that, in the picture, a small portion of the cones is also visible on the left. The agreement between simulation and experiment is very good, even if not all the simulated states were recorded by the camera.

3.7. Experimental Setup

In order to realize the two interlinked interactions from vacuum, we used the frequency-tripled continuous-wave mode-locked Nd:YLF laser regeneratively amplified described in Section 2.3 [58]. In particular, we exploited the third-harmonic pulse as the pump field a_{p1} to generate the spontaneous parametric downconversion process (interaction $k_{p1}^{e} = k_0^{o} + k_2^{o}$) and the fundamental pulse as the pump field a_{p2} to generate the

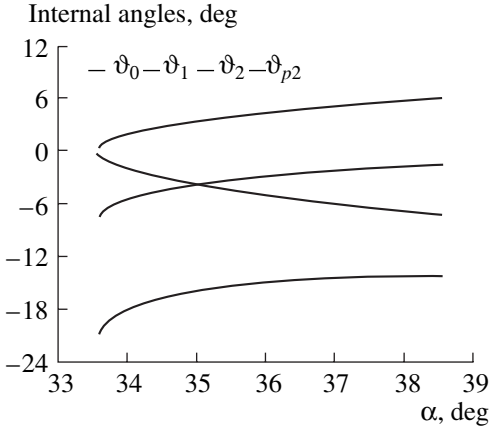

Fig. 20. Internal angles ϑ_j with $j = 0, 1, 2, p2$ as functions of the tuning angle α.

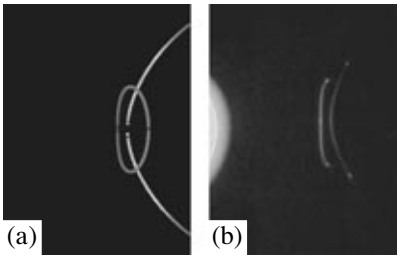

Fig. 21. (a) Simulated image of the two half-moons outside the crystal; (b) picture of the two half-moons.

sum-frequency between a portion of a cone and the infrared field itself (interaction $k_1^{e} = k_2^{o} + k_{p2}^{o}$).

For alignment purposes, we first realized the seeded process: to this end, we chose as the seed the light produced by a He–Ne continuous-wave laser (Melles-Griot, 5-mW max output power) at a wavelength of $\lambda_0 = 632.8$ nm. This choice allowed us to realize a nondegenerate interaction scheme in which the three evolving fields were at different frequencies with respect to each other or to the pumps, namely, $\lambda_0 = 632.8$ nm, $\lambda_1 = 446.4$ nm, and $\lambda_2 = 778.2$ nm.

As depicted in Fig. 22, the third harmonic extracted from the Nd:YLF laser was focused by lens f_{p1} of focal length 500 mm into a type-I BBO crystal (Fujian Castech Crystals, Fuzhou, China, $\vartheta_{CUT} = 34°$, cross-section of 10×10 mm and 4 mm in thickness) in order to generate the SPDC. Simultaneously, we sent the fundamental of the laser to the crystal at an of angle $\vartheta_{p2ext} = -34.8°$ with respect to the ultraviolet pump field (see Fig. 22). Since this field also emerges from the laser slightly divergent, we focused it by means of lens f_{p2} having a focal length of 500 mm. For alignment purposes, we used as seed field the light emitted by the He–Ne laser described above; we corrected the divergence

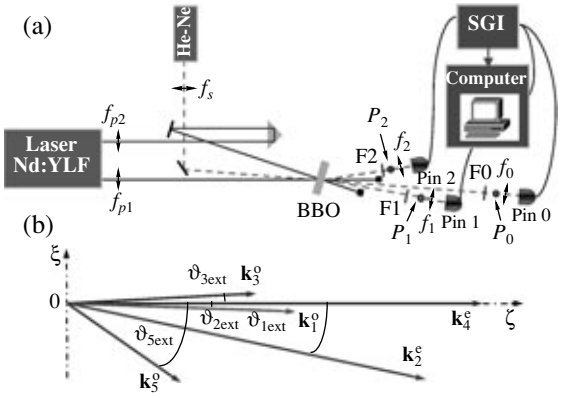

Fig. 22. (a) Experimental setup: BBO, nonlinear crystal; F0, F1, F2, cutoff filters; P_0, P_1, P_2, pinholes; $f_{0,\,1,\,2,\,p1,\,p2,\,s}$, lenses; Pin 0, 1, 2, *p–i–n* photodiodes; SGI, synchronous gated integrator. (b) Scheme of the interaction outside the crystal; $\vartheta_{j\text{ext}}$, external phase-matching angles; $\mathbf{k}_j^{o,\,e}$, wave vectors of the interacting fields.

of the beam by means of lens $f_s = 400$ mm, and then we sent it to the BBO with an external angle of $\vartheta_{0\text{ext}} = -2.54°$ with respect to the pump field a_{p1}.

By means of the two interlinked seeded interactions, we obtained two new fields, i.e., field a_2 ($\vartheta_2 = 3.35°$) generated by the difference frequency between the ultraviolet pump field and the seed field and then field a_1 ($\vartheta_1 = -12.78°$) produced by the sum-frequency between field a_2 and the infrared pump field. Note that, as the pump fields were sufficiently intense, the process starting from the vacuum also took place.

In order to check whether the generated fields belonged to an entangled triplet, we performed preliminary intensity correlation measurements among the generated fields. As for the TWB state, the position of the seeded spots is crucial for the correct selection of the twin coherence areas belonging both to the cones and to the half-moon. In order to choose the dimensions and the distances of the pinholes from the BBO, we followed a procedure analogous to that described for the TWB. However, it was not possible to study the dependence of the speckle dimensions on the pump energy, as this process, which involves two nonlinear interactions from the vacuum, is less efficient than the SPDC, and, thus, the CCD cannot resolve the coherent areas on the half-moon. Nevertheless, we analyzed the dependence of each of the three generated fields on the distance from the BBO, again represented by a direct linear proportionality. By taking into account this result, together with the fact that the divergence of the fields scales according to the ratio of the involved wavelengths, we assumed that, for an equal choice of the pinholes on two of the three fields, the ratio of the distances from the BBO must scale as the inverse ratio of the wavelengths. By exploiting this relation, we decided to place the detectors at three different distances from the crystal and to use pinholes having different dimensions. In particular, we put a pinhole with a size of 2.5 mm at a distance of 81 cm from the crystal to detect field a_0, a pinhole with a size of 2 mm at a distance of 72 cm to detect field a_1, and a pinhole with a size of 2 mm at a distance of 53.5 cm to detect field a_2. The light was suitably filtered before each pinhole and focused on each *p–i–n* photodiode (Pin 0, 1, 2 in Fig. 22) by a lens ($f_0 = f_1 = 25$ mm, $f_2 = 50$ mm) located just beyond the spatial selector. The overall quantum efficiencies of the detection branches were $\eta_0 = 0.44$, $\eta_1 = 0.72$, and $\eta_2 = 0.43$. As for the TWB, each current output was integrated over a synchronous gate of suitable time duration (40 ns) by a synchronous gated integrator (SGI) in external trigger modality; each SGI output was then digitized by a 13-bit converter (SR250, Stanford Research Systems, with 50-mV full scale), and the counts were stored in a PC-based multichannel analyzer.

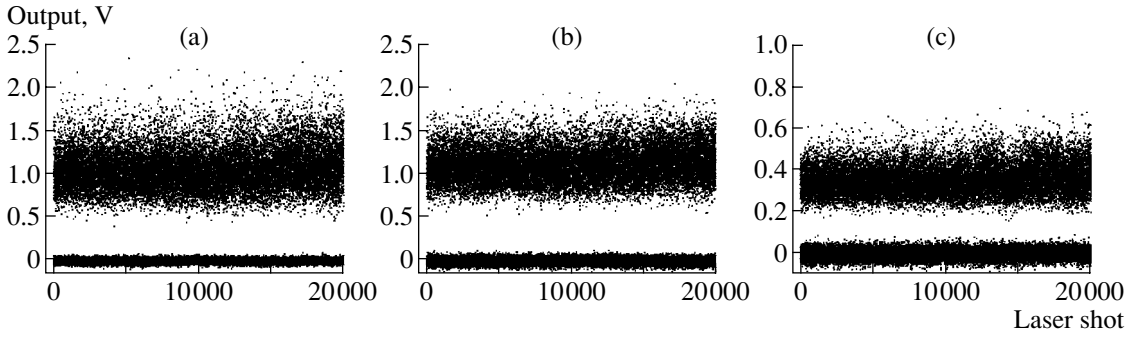

Fig. 23. (a) Output voltages for the beam at $\lambda_0 = 632.8$ nm for a sequence of laser shots and noise (from a separate measurement in the dark). (b) Output voltages for the beam at $\lambda_2 = 778.2$ nm for the same sequence of laser shots and noise. (c) Output voltages for the beam at $\lambda_1 = 446.4$ nm for the same sequence of laser shots and noise.

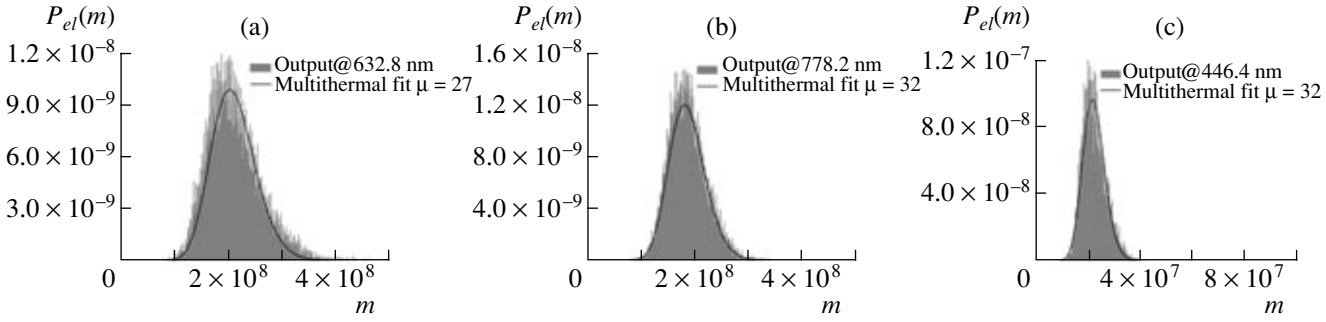

Fig. 24. (a) Histogram of the intensity distribution of the beam at $\lambda_0 = 632.8$ nm together with the multithermal fit. (b) Histogram of the intensity distribution of the beam at $\lambda_2 = 778.2$ nm together with the multithermal fit. (c) Histogram of the intensity distribution of the beam at $\lambda_1 = 446.4$ nm together with the multithermal fit.

3.8. Experimental Results

In Figs. 23a–23c, we show the recorded outputs of the photodiodes for a sequence of laser shots, together with the noise of the detectors. In particular, the traces of the three generated fields have a variance characteristic of multithermal statistics. In fact, the corresponding normalized probability distributions reported in Figs. 24a–24c for the same data are well fitted by multithermal distributions obtained by the convolution of μ equally populated thermal modes. In this case, the number of modes for the three fields is given by 27 temporal modes in the coherence area of field a_0, 32 temporal modes in the coherence area of field a_1, and 32 temporal modes in the coherence area of field a_2.

A preliminary criterion to identify the three parties of the triplet is given by the calculus of the correlation function (see Eq. (48)); however, it represents a necessary but not sufficient condition to establish the entangled nature of the three modes [58].

Moreover, we have to remember that, according to Eq. (63), by taking the vacuum as the initial state, at any time $t \neq 0$, the mean photon number on mode a_0 is the sum of the mean photon numbers on modes a_1 and a_2. The coherence areas are thus correctly selected when the correlation coefficient ε (see Eq. (49)) between the photons detected on mode a_0 and the sum of the photons detected on the other two modes is maximum.

In the case of multithermal statistics, the correlation coefficient for the three-mode state can be written as follows:

$$\varepsilon_{\mathrm{TRI}} = \frac{\eta_0(1 + N_1 + N_2)(\eta_1 N_1 + \eta_2 N_2)}{(\sigma_0^2 \delta^2)^{1/2}}, \qquad (117)$$

in which

$$\sigma_0^2 = \eta_0(N_1 + N_2)[1 + \eta_0(N_1 + N_2)], \qquad (118a)$$

$$\delta_0^2 = (\eta_1 N_1 + \eta_2 N_2)(1 + \eta_1 N_1 + \eta_2 N_2). \qquad (118b)$$

Note that, in the limit of intense fields, $\varepsilon_{\mathrm{TRI}}$ approaches unity for any value of η_j.

In Fig. 25, we show the correlation function for the detected photons plotted as a function of the delay in the laser shots. Note that the experimental correlation coefficient is ε = 0.914 and that subsequent shots result to be uncorrelated. The correlation is smaller than the theoretical unit value. In order to reduce the added noise, we will modify the experimental conditions to improve the selection of the coherence areas. Moreover, we will exploit the remarkable flexibility of the interacting scheme realized in a single crystal to choose the best conditions for detecting the outputs and for eliminating the presence of spurious light that would impinge on the detectors in spite of the filters. Finally, in order to verify the existence of quantum correlations, we may implement measurements at a lower number of detected photons, with a suitable change of the detection chain in order to reduce the detection noise. An alternative interaction scheme will also be used, in which the interlinked interactions will take place in two distinct nonlinear crystals in a cascading geometry: this should help in finding the correlated parties of the triplets.

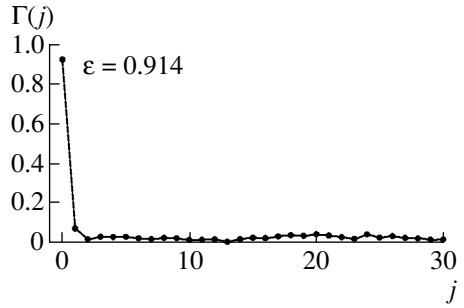

Fig. 25. Correlation function between the photons detected on field a_0 and the sum of photons detected on fields a_1 and a_2 as a function of the delay between the laser shots.

4. CONCLUSIONS

In this paper, we have analyzed in detail three- and five-mode parametric interactions in $\chi^{(2)}$ crystals, reviewing their description and applications. Concerning three-wave interactions, we have derived classical equations of motion and then solved them within the parametric approximation, taking into account phase mismatching both in modulus and direction. Moreover, we have considered the corresponding two-mode quantum model obtained under phase-matching conditions. The evolution from the vacuum or from a coherent seed signal has been explicitly evaluated, and the resulting entangled states have been characterized. The conditions for the experimental generation of a twin beam by type-I nonlinear interactions in a noncollinear phase-matching geometry in BBO crystals have been discussed, and the experimental results obtained for the photon distribution, as well as for the photon correlation, have been reported.

Five-mode interactions taking place in a single crystal have also been considered. In particular, we focused on schemes employing type-I noncollinear phase-matching geometry, which provides remarkable flexibility in the choice of experimental parameters. Classical equations of motion have been derived and solved under phase-matching conditions and within the parametric approximation, showing that, for a single seed signal at the crystal input, two holographic replicas should be expected at the output. Experimental results are also reported confirming the holographic properties in very good agreement with the theory. In addition, the implementation of several kinds of all-optical devices, such as logic gates, looping circuits, and switches, is analyzed both theoretically and experimentally, showing an excellent optical resolution due to the holographic nature of the process. The generation of entanglement by three-mode bilinear interactions in the quantum regime has been extensively described and discussed, also illustrating a possible application in the implementation of a $1 \longrightarrow 2$ telecloning protocol. The experimental realization of five-wave interactions has been demonstrated using the fundamental and third harmonics of a continuous-wave mode-locked Nd:YLF laser as the pump fields. Experimental results for the photon correlations show a good agreement with the theory.

We conclude that parametric interactions in $\chi^{(2)}$ crystals represent powerful tools for the optical manipulation of information both in the classical and the quantum regimes.

ACKNOWLEDGMENTS

The authors thank A. Andreoni for encouragement and support. This work has been supported by MIUR through project nos. PRIN-2005024254-002 and FIRB RBAU014CLC-002. This work arises in part from the Ph.D. research program of A.A. and A.F. A.F. acknowledges financial support from Università di Milano under the grant "Borse di perfezionamento all'estero."

REFERENCES

1. J. A. Armstrong, N. Bloembergen, J. Ducuing, and P. S. Pershan, Phys. Rev. **127**, 1918 (1962).
2. S. A. Akhmanov, A. I. Kivrigin, A. S. Piskarskas, et al., Pis'ma Zh. Eksp. Teor. Fiz. **2**, 300 (1965) [JETP Lett. **2**, 191 (1965)].
3. P. Franken, A. E. Hill, C. W. Peters, and G. Weinreich, Phys. Rev. Lett. **7**, 118 (1961).
4. L. Mandel and E. Wolf, *Optical Coherence and Quantum Optics* (Cambridge Univ. Press, Cambridge, 1995; Fizmatlit, Moscow, 2000).
5. J. Peřina, *Quantum Statistics of Linear and Nonlinear Optical Phenomena* (Kluwer, Dordrecht, 1991; Mir, Moscow, 1987).
6. G. M. D'Ariano, Int. J. Mod. Phys. B **6**, 1292 (1992).
7. H. P. Yuen, Phys. Rev. A **13**, 2226 (1976).
8. Y. Yamamoto and H. A. Haus, Rev. Mod. Phys. **58**, 1001 (1986).
9. "Special Issues on Squeezed States," Ed. by H. J. Kimble and D. F. Walls, J. Opt. Soc. Am. B, **4** (1987); Ed. by R. Loundon and P. L. Knight, J. Mod. Opt. **34** (1987).
10. *Quantum Interferometry*, Ed. by F. De Martini et al. (VCH, Wenheim, 1996), pp. 95–224.
11. C. O. Alley and Y. H. Shih, Phys. Rev. Lett. **61**, 2921 (1988).
12. Z. Y. Ou and L. Mandel, Phys. Rev. Lett. **61**, 50 (1988).
13. J. G. Rarity and P. B. Tapster, Phys. Rev. Lett. **64**, 2495 (1990).
14. G. M. D'Ariano and M. F. Sacchi, Phys. Rev. A **52**, R4309 (1995).
15. D. Boschi, F. De Martini, and G. Di Giuseppe, in *Quantum Interferometry*, Ed. by F. De Martini et al. (VCH, Wenheim, 1996), pp. 135–143.
16. D. N. Klyshko, Phys. Lett. A **132**, 299 (1988).
17. M. A. Horne, A. Shimony, and A. Zeilinger, Phys. Rev. Lett. **62**, 2209 (1989).
18. A. Bandilla, G. Drobný, and I. Jex, Phys. Rev. Lett. **75**, 4019 (1995); Phys. Rev. A **53**, 507 (1996); Opt. Comm. **128**, 353 (1996).
19. B. R. Mollow and R. J. Glauber, Phys. Rev. **160**, 1076 (1967); **160**, 1097 (1967).
20. G. M. D'Ariano, M. G. A. Paris, and M. F. Sacchi, Nuovo Cimento B **114**, 339 (1999).
21. D. R. Truax, Phys. Rev. D **31**, 1988 (1985).
22. M. Ban, J. Opt. Soc. Am. B **10**, 1347 (1993).
23. M. E. Smithers and E. Y. C. Lu, Phys. Rev. A **10**, 1874 (1974).
24. R. R. Puri, Phys. Rev. A **50**, 5309 (1994).
25. C. M. Caves and B. L. Schumaker, Phys. Rev. A **31**, 3068 (1985).
26. B. E. A. Saleh and M. C. Teich, *Fundamentals of Photonics* (Wiley, New York, 1991), Chap. 19.
27. V. G. Dmitriev, G. G. Gurzadyan, and D. N. Nikogosyan, *Handbook of Nonlinear Optical Crystals* (Springer, Berlin, 1991).

28. M. Bondani and A. Andreoni, Phys. Rev. A **66**, 0338051 (2002).
29. M. Bondani, A. Allevi, and A. Andreoni, J. Opt. Soc. Am. B **20**, 1 (2003).
30. A. Ferraro, S. Olivares, and M. G. A. Paris, *Gaussian States in Quantum Information* (Bibliopolis, Napoli, 2005).
31. R. Simon, E. C. G. Sudarshan, and N. Mukunda, Phys. Rev. A **36**, 3868 (1987); R. Simon, N. Mukunda, and B. Dutta, Phys. Rev. A **49**, 1567 (1994).
32. R. Simon, Phys. Rev. Lett. **84**, 2726 (2000).
33. F. Paleari, A. Andreoni, G. Zambra, and M. Bondani, Opt. Express **12**, 2816 (2004).
34. A. Agliati, M. Bondani, A. Andreoni, et al., J. Opt. B **7**, S652 (2005).
35. M. Bondani, A. Allevi, E. Puddu, et al., Opt. Lett. **29**, 180 (2004).
36. J. W. Goodman, *Introduction to Fourier Optics* (McGraw-Hill, New York, 1988; Mir, Moscow, 1970).
37. A. Andreoni, M. Bondani, M. C. A. Potenza, et al., Rev. Sci. Instrum. **72**, 2525 (2001).
38. E. Puddu, A. Allevi, A. Andreoni, and M. Bondani, J. Opt. Soc. Am. B **21**, 1839 (2004).
39. E. A. Mishkin and D. F. Walls, Phys. Rev. **185**, 1618 (1969); M. E. Smithers and E. Y. C. Lu, Phys. Rev. A **10**, 1874 (1974).
40. A. Ferraro, M. G. A. Paris, M. Bondani, et al., J. Opt. Soc. Am. B **21**, 1241 (2004).
41. A. S. Bradley, M. K. Olsen, O. Pfister, et al., Phys. Rev. A **72**, 053805 (2005); R. C. Pooser and O. Pfister, Opt. Lett. **30**, 2635 (2005).
42. A. V. Rodionov and A. S. Chirkin, JETP Lett. **79**, 582 (2004).
43. J. Guo et al., Phys. Rev. A **71**, 034305 (2005).
44. M. K. Olsen and A. S. Bradley, J. Phys. B: At. Mol. Opt. Phys. **39**, 127 (2006).
45. N. Piovella, M. Cola, and R. Bonifacio, Phys. Rev. A **67**, 013817 (2003).
46. S. Pirandola, S. Mancini, D. Vitali, and P. Tombesi, Phys. Rev. A **68**, 062317 (2003).
47. G. X. Li, S. P. Wu, and G. M. Huang, Phys. Rev. A **71**, 063817 (2005).
48. P. van Loock and S. L. Braunstein, Phys. Rev. A **63**, 022106 (2001).
49. A. Ferraro and M. G. A. Paris, J. Opt. B **7**, 174 (2005).
50. P. van Loock and S. L. Braunstein, Phys. Rev. Lett. **84**, 3482 (2000).
51. T. Aoki, N. Takei, H. Yonezawa, et al., Phys. Rev. Lett. **91**, 080404 (2003); H. Yonezawa, T. Aoki, and A. Furusawa, Nature **431**, 430 (2004).
52. P. van Loock and S. L. Braunstein, Phys. Rev. Lett **87**, 247901 (2001).
53. A. Ferraro and M. G. A. Paris, J. Opt. B: Quantum Semiclass. Opt. **7**, 532 (2005).
54. M. Murao, D. Jonathan, M. B. Plenio, and V. Vedral, Phys. Rev. A **59**, 156 (1999).
55. N. J. Cerf, A. Ipe, and X. Rottenberg, Phys. Rev. Lett. **85**, 1754 (2000).
56. J. Fiurášek, Phys. Rev. Lett. **86**, 4938 (2001); N. J. Cerf, S. Iblisdir, and G. Van Assche, Eur. Phys. J. D **18**, 211 (2002).
57. A. Ferraro and M. G. A. Paris, Phys. Rev. A **72**, 032312 (2005).
58. M. Bondani, A. Allevi, E. Gevinti, et al., quant-ph\0604002.
59. Indeed, the evolution of a state via Hamiltonians at most bilinear in the field's operators corresponds to a symplectic transformation of the covariance matrix. Since the covariance matrix of the vacuum and of a coherent state is the same, we conclude that the states $|\Psi_2\rangle$ and $|\Psi_{2,\alpha}\rangle$ have the same covariance matrix.